Politecnico di Milano

Scuola di Ingegneria Industriale e dell'Informazione

Corso di laurea magistale in Ingegneria Biomedica

SOFT ROBOTIC SKIN FOR INTRAOPERATIVE IDENTIFICATION OF PROSTATE CANCER

Relatore: Elena DE MOMI PhD.

Correlatore: Pietro VALDASTRI PhD.

Marco BECCANI

Tesi di Laurea di:

Federico CAMPISANO Matr. 799399

Anno Accademico 2013-2014

grazie a Marco, Addisu, Piotr e a tutti i colleghi allo STORM lab
grazie a Nick per i tanti momenti passati insieme,
grazie ai miei amici/colleghi a Milano,
un sentito grazie a Pietro per tutto, e infine
soprattutto grazie ai miei genitori che hanno reso tutto questo possibile.

Contents

List of Figures

List of Tables

Sommario

INTRODUZIONE

Il cancro alla prostata é il secondo piú comune cancro negli uomini. Si stima che circa 1.1 milioni di uomini nel mondo hanno avuto una diagnosi di cancro alla prostata nel 2012, pari al 15 % di tutti i tumori diagnosticati negli uomini, con quasi il 70 % di questi casi (759 mila) che si verificano nelle regioni piú sviluppate [12].

In genere, gli uomini con cancro alla prostata in fase precoce ricorrono alla prostatectomia, che consiste nella la rimozione chirurgica della ghiandola prostatica. Nel 2010, 138.000 prostatectomie sono state eseguite solamente negli Stati Uniti.

Quando la prostatectomia viene eseguita in chirurgia aperta, il chirurgo puó farsi aiutare dal feedback tattile per identificare il tumore dal tessuto sano circostante, dato che la zona neoplastica é solitamente piú rigida rispetto al tessuto normale. Tuttavia, ad oggi questo tipo di operazioni viene sempre piú eseguito con tecniche mini-invasive (ad esempio, 4 su 5 prostatectomie radicali negli Stati Uniti vengono eseguite tramite la chirurgia mini-inzvasiva robotica [24]). In queste procedure, il chirurgo ha la minima o nessuna interazione tattile con il tessuto. Un approccio con chirurgia mini-invasiva riduce il tempo di recupero per il paziente, ma pone una sfida rilevante: l'individuazione del tumore rispetto ai tessuti e strutture nervose che lo circondano. In particolare, i fasci neurovascolari

che si trovano su entrambi i lati della prostata e innervano importanti funzioni urogenitali come erezione e controllo della vescica.

Sebbene la prostatectomia é una procedura efficace a sradicare il cancro, gli effetti collaterali come incontinenza urinaria e la disfunzione erettile possono gravemente incidere sulla qualitá della vita dei pazienti nel periodo post-operatorio. L'incidenza di questi effetti collaterali é di circa il 22 % [16], quindi ogni sforzo per migliorare la preservazione dei nervi durante la prostatectomia minimamente invasiva é altamente significativo. In particolare, il ripristino di sensazioni tattili sarebbe fondamentale per definire i margini del tumore alla prostata, guidando cosí una resezione completa senza rinunciare al tessuto normale in eccesso e preservare i fasci neurovascolari in modo piú efficiente.

In questo spirito, proponiamo un nuovo approccio per la palpazione del tessuto, dove una Soft Robotic Skin (SRS) é inserita attraverso un trocar laparoscopico, ancorata sulla prostata per accoppiamento magnetico, e fatta operare durante l'intervento senza richiedere l'assistenza del chirurgo con lo scopo di creare una mappa della rigiditá meccanica del prostata. Come primo passo in questa direzione, il presente lavoro di ricerca si concentra sulla parte sensibile della SRS e affronta la progettazione , modellazione , fabbricazione , calibrazione e la caratterizzazione di una pelle sensorizzata flessibile che contiene una matrice di sensori di pressione e puó creare un'immagine tattile della prostata.

MATERIALI AND METODI

Come rappresentato in Fig.1, la SRS é introdotta in sala operatoria attraverso una incisione chirurgica o attraverso un trocar laparoscopico prima che la prostatectomia abbia inizio. Un modulo di ancoraggio rettale permette di mantenere stabile intorno alla prostata . Una volta in

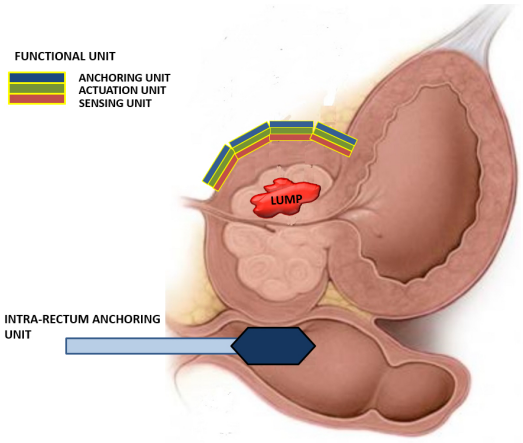

Figure 1: Principio di funzionamento per la palpazione di tessuto con la Soft Robotic Skin (SRS)

posizione, il controllore insuffla delle camere d'aria presenti dietro ogni modulo sensibile della pressione necessaria per palpare il tessuto e creare una mappa di distribuzione della rigiditá meccanica. Questa mappa, identifica idealmente regioni piú rigide nella prostata, e pu quindi guidare la resezione del tumore, preservando i fasci neurovascolari e riducendo cosí le possibilitá di complicazioni.

Prima di progettare l'unitá di ancoraggio e le parti di attuazione della SRS, é necessario dimostrare la fattibilitá nell'identificazione di tumori in un campione di tessuto morbido che simula la prostata. Con questo obiettivo in mente, questo lavoro di tesi ha affrontato i seguenti passi:

- **Selezione dei sensori**: Sensori di pressione barometrica MEMS sono stati adottati per affrontare i problemi legati alle dimensioni e ai vincoli di flessibilitá della SRS. Il sensore una volta inglobato nel silicone presenta una buona sensibilitá, riduce al minimo le dimensioni del device finale e permette l'integrazione con un elevato numero di sensori nello stesso array.

- **Modellazione**: Il modello di Kelvin-Voight per i materiali vis-

coelastici é stato adottato per correlare le uscite del sensore alle proprietá del silicone e del tessuto che simula la prostata. La rigiditá locale del tessuto é stata stimata confrontando la pressione imposta con la pressione misurata dai sensori.

- **Stima del Cross-talk**: esperimenti preliminari sono stati condotti per definire la minima distanza in cui due sensori adiacenti hanno uscite in pressione non correlate tra loro. Ció ha consentito di minimizzare il numero di sensori di pressione all'interno della SRS.

- **Fabricazione**:Un totale di venti sensori sono stati saldati su una scheda flessibile di circuito stampato (PCB) divisa in 5×4 tasselli connessi tra loro da connessioni flessibili. Ogni tassello ha la funzione di unitá sensibile e puó lavorare in unione con gli altri. Il circuito flessibile é stato inglobato nel silicone seguendo diversi step di stampo e di degassamento.

- **Sviluppo dell'algoritmo di sensing**: L'algoritmo é stato sviluppato con l'obbiettivo di controllare in real-time una matrice di 5×4 sensori. La performance é stata dopo testata per assicurare l'affidabilitá della pressione letta dal sensore.

- **Calibrazione**: Ogni singolo tassello é stato calibrato usando una load cell connessa ad un manipolatore robotico che forniva sempre la stessa indentazione controllata. Ogni coefficiente é stato derivato dalla combinazione del modello con i dati sperimentali.

- **Caratterizzazione**: la precisione di ogni singolo tassello e dell'intera pelle sensibile sono stati valutati tramite prove sperimentali. Un phantom con nove tumori con differenti diametri e inglobati a diverse profonditá é stato utilizzato per valutare la performance della

pelle. Lo stesso setup é stato utilizzato anche per quantificare la risoluzione spaziale e valutare la rigiditá del tessuto. Infine, la pelle é stata testata da un chirurgo che ha eseguito la palpazione di un tessuto con tre tumori inglobati all'interno di un simulatore per laparoscopia.

Una immagine della pelle é mostrata in Fig.2. Le dimensioni sono $104mm \times 70mm$. Grazie alla sua flessibilitá, la pelle puó essere arrotolata per entrare da una incisione di $2cm$.

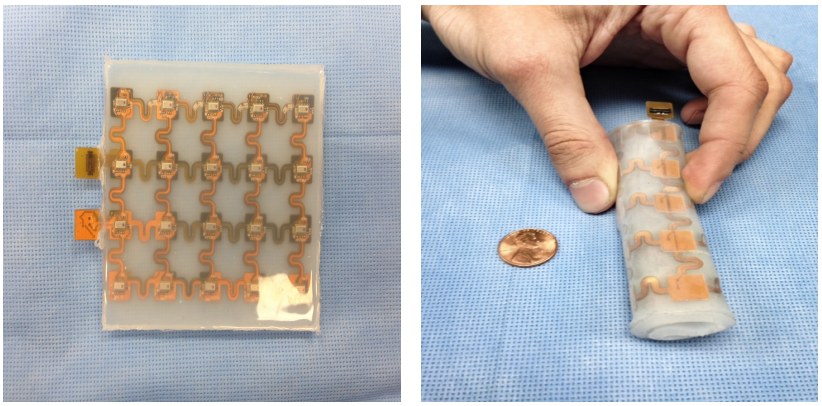

Figure 2: a) Pelle sensibile che ingloba 20 sensori di pressione, b) arrotolata per entrare da una incisione di 2 cm)

RISULTATI

La pelle sensible ha riportato questi risultati:

- **Sensitivitá del singolo tassello**: La sensitivitá di ogni tassello é dell'ordine di un grammo-forza (0.01N), mentre la deviazione standard media a causa del rumore é circa 0.01 grammi forza (0.001N).
- **Risoluzione Spaziale**: la risoluzione spaziale media per ogni tassello é di $56mm^2$ che corrisponde a un raggio di 4,2 mm quando il modulo viene posto su un supporto rigido, e diventa $1256mm^2$

quando la pelle sonda un campione di tessuto, corrispondente ad un raggio di 2 cm.

- **Accuratezza**: il modello Kelvin-Voight puó essere usato per descrivere il comportamento del sistema con una accuratezza di 4 % FS . I dati dopo la calibrazione hanno mostrato una accuratezza di 0,01 % FS.

- **Frequenza di aggiornamento**: l'algoritmo di campionamento é in grado di acquisire dati da tutta la matrice ad una velocitá di campionamento di 100Hz e presentarli su un'interfaccia utente in tempo reale.

- **Mappa meccanica della rigiditá del tessuto**: Il tasso complessivo di individuazione con successo del tumore in tutti gli esperimenti di questa tesi é 81% con un errore complessivo di identificazione della posizione di $E_x = 1.85mm$ and $E_y = 0.85mm$, che corrisponde a 0.09% e 0.04% di errore relativo, rispettivamente. I tumori con un diametro di 10mm e 8 mm sono sempre stati identificati indipendentemente dalla profonditá con un errore relativo complessivo nella stima dell'area di 35% e 23%, rispettivamente. I tumori di 6 mm di diametro sono stati identificati con un tasso complessivo di 25% negli esperimenti, ma i dati non sono stati affidabili per stimare l'area. La pressione di input adottata per questi trial é stata 55 kPa. Le immagini corrispondenti ai risultati sono Fig.3 e 4.

DISCUSSIONE

I risultati di questa tesi dimostrano che é possibile utilizzare la pelle sensibile per rilevare tumori incorporati nel tessuto molle che sono al piú

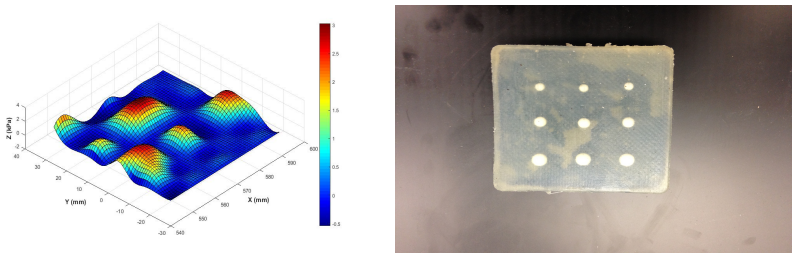

Figure 3: Riconoscimento di tumori nel tessuto: Il tasso di successo nel rilevamento del tumore all'interno del tessuto é 77%

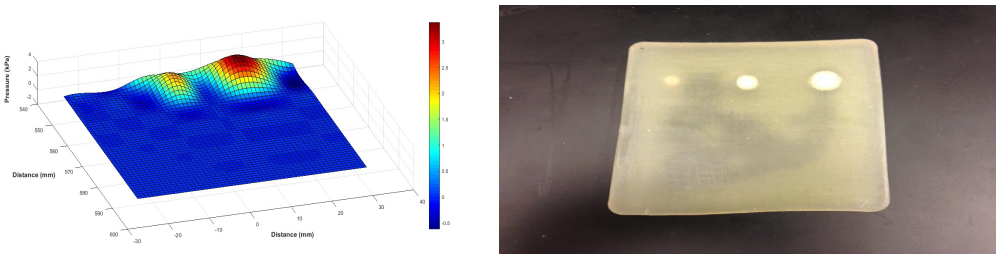

Figure 4: Riconoscimento di tumori nel tessuto in un MIS training box: Il tasso di successo nel rilevamento del tumore all'interno del tessuto é 66%

piccoli 6 mm di diametro. Come previsto, piú il tumore é grande e vicino alla superficie, piú é semplice rilevarlo.

Il semplice modello viscoelastico ha dimostrato di predire il comportamento del sistema con un errore relativamente piccolo. Un successivo passo sarebbe espandere la modellazione e inserire parametri di progetto quali lo spessore degli strati di silicone, le proprietá del materiale, il passo e la posizione del sensore, ecc. Questo consentirebbe di ottimizzare la progettazione e di adattarla ai differenti tessuti e a diverse geometrie di organo.

Questo studio ha anche identificato la pressione che l'unitá di attuazione del SRS dovrebbe fornire al modulo di sensing, il potenziale di cross-talk tra i tasselli, e i protocolli per la fabbricazione della pelle e

la calibrazione. Tutto questo lavoro servirá come sfondo per lo sviluppo di una Soft Sobotic Skin completa per la mappatura intraoperatoria della rigiditá meccanica della prostata, con il potenziale di migliorare i risultati della prostatectomia in chirurgia minimamente invasiva.

Abstract

INTRODUCTION

PROSTATE cancer is the second most common cancer in men. An estimated 1.1 million men worldwide were diagnosed with prostate cancer in 2012, accounting for 15% of the cancers diagnosed in men, with almost 70% of the cases (759,000) occurring in more developed regions [12].

Typically, men with early-stage prostate cancer are referred to prostatectomy, i.e. the surgical removal of the prostate gland. In 2010, 138,000 prostatectomies were performed in the United States alone.

When prostatectomy is performed in open surgery, the surgeon can rely on tactile feedback to identify the cancer from the surrounding healthy tissue, as the neoplastic area is stiffer than normal. However, more and more procedures are performed with minimally invasive techniques (e.g., 4 out of 5 radical prostatectomies in the United States are performed via robotic minimally invasive surgery [24]). In these procedures, the surgeon has minimal or no tactile interaction with the tissue. A minimally invasive approach shortens the recovery time for the patient, but poses relevant challenges in the effective identification of the tumor with respect to the tissues and nerve structures surrounding it. In particular, the neurovascular bundles that lie to either side of the prostate innervate important genitourinary functions such as erection and detrussor control.

Although prostatectomy is effective at eradicating the cancer, the side effects of urinary incontinence and erectile dysfunction can severely affect quality of life for post-operative patients. The incidence of these side effects is about 22% [16]., therefore any effort in improving nerve sparing during minimally invasive prostatectomy is highly significant. In particular, restoring tactile sensations would be crucial to define prostate tumor margins, thus guiding a complete resection without sacrificing excess normal tissue and preserving the neurovascular bundles more efficiently.

In this spirit, we propose a novel tissue palpation approach, where a soft robotic skin (SRS) is deployed through a standard trocar, docked on the prostate by magnetic coupling, and operated without requiring surgical assistance to intraoperatively create a mechanical stiffness map of the prostate. As a first step in this direction, the present research work focuses on the sensitive part of the SRS and addresses the design, modeling, fabrication, calibration, and characterization of a flexible skin that contains an array of pressure sensors and can create a tactile image of the prostate.

MATERIALS AND METHODS

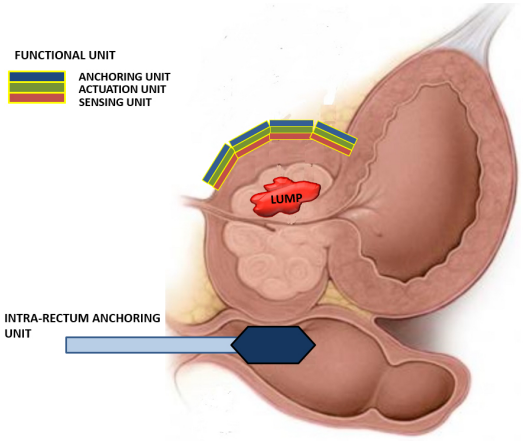

Figure 5: Principle of operations for tissue palpation using a Soft Robotic Skin (SRS)

As represented in Fig.5, the SRS is introduced in the operating theater via a surgical incision or through a trocar before prostatectomy. It is then coupled with a rectal anchoring module via magnetic field to hold a stable position around the prostate. Once in place, a pneumatic actuation module insufflates a chamber behind each pressure sensitive module to palpate the tissue and create a mechanical stiffness distribution map. This map, ideally identifying stiffer regions in the prostate, should then guide tumor resection while improving nerve sparing and reducing the chances of complications.

Before designing the anchoring and the actuation parts of the platform, it is necessary to demonstrate the feasibility of identifying lumps in a soft tissue sample with a flexible/stretchable array of pressure sensors embedded in a soft silicone rubber. With this goal in mind, this thesis work addressed the following steps:

- **Sensors selection**: A MEMS barometric pressure sensor was adopted to address the size and flexibility constraints of the SRS. This selection guaranteed an adequate range of sensitivity, while minimizing dimensions and allowing integrating a high number of sensors in a small footprint.

- **Modeling**: the Kelvin-Voight model for viscoelastic material was adopted to relate the sensor outputs to the material properties of the silicone rubber and the tissue in contact with the sensitive skin. The local stiffness of the tissue was estimated by comparing the imposed indentation pressure and the pressure measured by the sensors.

- **Cross-talk estimation**: preliminary experiments were performed to define the pitch for the sensor array in a way that cross talk between neighbouring sensors was not affecting the readouts. This

allowed to minimize the number of pressure sensors to cover the area of the SRS.

- **Fabrication**: A total of twenty sensors were soldered on a flexible printed circuit board (PCB) divided into 5×4 taxels connected by flexible wires. Each taxel has the function of a sensitive unit and can work in conjunction with all the other units. The flexible circuit was embedded in a silicone rubber via a procedure involving multiple molding/degasing steps.

- **Sensing algorithm development**: The sensing algorithm was developed with the purpose of controlling in real-time a matrix of 5×4 sensors and its performance was tested to ensure the reliability of data sampling.

- **Calibration**: each single taxel was calibrated using a load cell connected to a robotic manipulator, which was providing a controlled indentation pressure. Each calibration coefficient was derived by combining the model with the experimental data.

- **Characterization**: the accuracy of each single taxel and of the entire sensitive skin were evaluated via experimental trials. A tissue simulator embedding nine lumps with different diameters at different depths was used to assess the ability of the flexible skin in detecting tumoral masses. The same setup was used also to quantify the spatial resolution of the stiffness map created by the proposed method. Finally, a surgeon performed tissue palpation by using the sensitive skin and a tissue simulator inside a laparoscopic training simulator.

A picture of the sensing module embedding twenty pressure sensitive elements is represented in Fig.6. The size is $104mm \times 70mm$. Thanks to

its flexibility, the skin can be wrapped to enter from a $2 - cm$ incision.

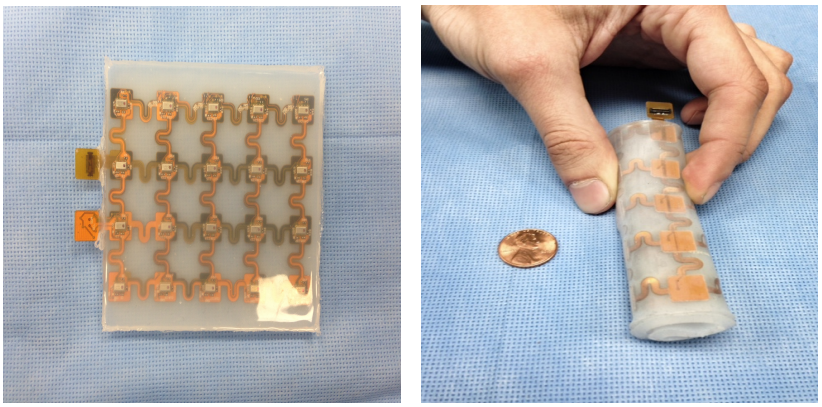

Figure 6: a) Sensting sub-module embedding twenty pressure sensitive elements, b) wrapped to enter from a 2 cm incision)

RESULTS

The sensitive skin reported the following performances:

- **Taxel sensitivity**: the sensitivity for each taxel was in the order of one gram-force (0.01 N), while the average standard deviation due to the noise was about 0.01 gram-force (0.001N).
- **Spatial resolution**: the average spatial resolution for each taxel was $56mm^2$ that corresponds to a radius of 4.2 mm when the module is placed on a rigid support, and becomes $1256mm^2$ when probing a tissue sample, corresponding to a radius of 2 cm.
- **Accuracy in stiffness reconstruction**: the Kelvin-Voight model can be used to describe the behavior of the system with an accuracy of 4% FS. The data after calibration showed an accuracy of 0.01% FS.

- **Refresh rate**: the sensing algorithm was able to acquire data at a sampling rate of 100Hz and present them on a graphical user interface in real time.

- **Mechanical stiffness mapping**: The overall lump detection success rate in all the experiments performed in this thesis was 81% with an overall error in lump position identification of $E_x = 1.85mm$ and $E_y = 0.85mm$, corresponding to 0.09% and 0.04% of relative error, respectively. The lumps with a diameter of 10 mm and 8 mm were always identified independently of the depth with an overall relative error in estimating the area of 35% and 23%, respectively. The 6 mm lumps were identified with an overall rate of 25%, but the data were not reliable enough to estimate their area. The indentation pressure adopted for these trials was 3mm. Pictures related to the results for the mechanical stiffness mapping trials are reported in Fig.7 and 8.

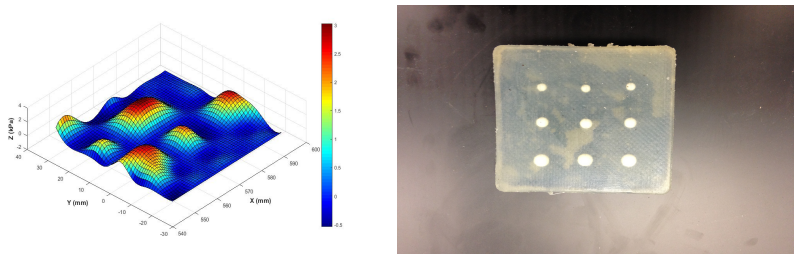

Figure 7: Lump detection on a phantom tissue: The resulting average resulting lump detection success rate was equal to 77%

DISCUSSION

The results of this thesis show that it is possible to use a flexible sensitive skin to detect lumps embedded in soft tissue that are as small as

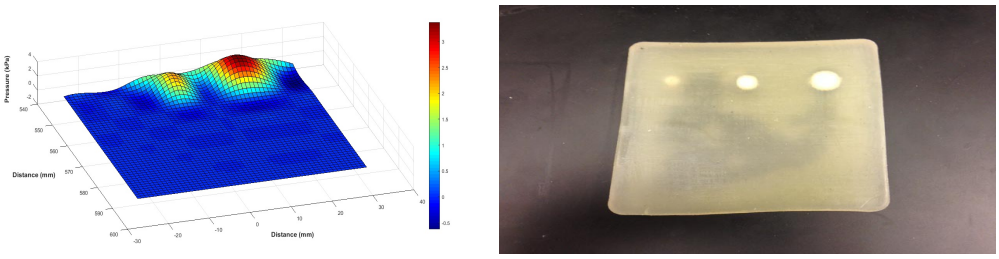

Figure 8: Lump detection on a MIS training box: The resulting average lump detection success rate was equal to 66%

6 mm in diameter. As expected, the larger is the lump and the closer is to the tissue surface, the easier is to detect it. To improve the performance of the sensitive skin even further, a thinner layer of silicone rubber can be used.

The simple viscoelastic model has shown to predict the behavior of the system with a relatively small error. A next possible step would be to expand the modeling to include design parameters such as the thickness of the silicone layers, the material properties, the sensor pitch and location, etc. This would allow to optimize the design and to adapt it to different tissues and different organ geometries.

This study also identified the desired indentation pressure that the actuation unit of the SRS should provide, the potential for cross talk between taxels, and the protocols for skin fabrication and calibration. All this body of work will serve as background for the implementation of a complete soft robotic skin for intraoperative mapping of the mechanical stiffness of the prostate, with the potential of improving the outcomes of minimally invasive prostatectomy.

Chapter 1

Introduction

1.1 Prostate: Anatomy and Physiology

The prostate is a pyramidal fibromuscular gland found in the pelvis. It lies at a low level in the lesser pelvis, behind the inferior border of the symphysis pubis and pubic arch, and anterior to the rectourethralis and rectal ampulla, Fig.1.1.

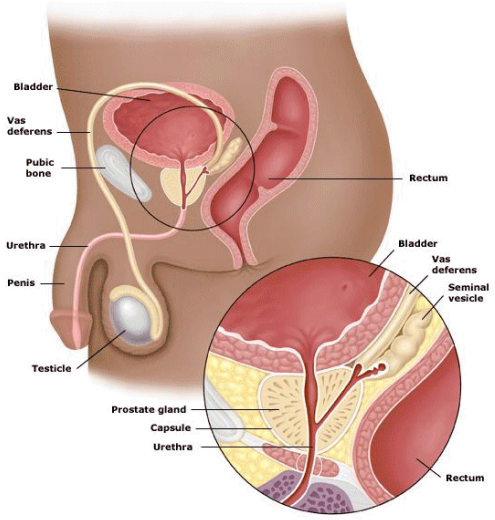

Figure 1.1: Location of the prostate

On the superior side, the prostate is closely related to the neck of the

bladder [1]. It is oval shaped with a rounded tip. It is approximately 4 cm wide and 3 cm thick. The actual size of the prostate varies from man to man. It can range from the size of a walnut to a small apple [2].

There are several structures closely related to the prostate that need consideration when contemplating prostatectomy. The most important of which is the neurovascular bundle (NVB). The NVB is composed of numerous nerve fibers superimposed on a scaffold of veins, arteries, and variable amounts of adipose tissue. The bundle is located dorsally and laterally to both sides of the prostate. The NVB is responsible for the mechanisms of erection, ejaculation, and urinary continence, which is the predominant issue post-prostatectomy [3]. Preserving these bundles can significantly improve quality of life after surgery [4].

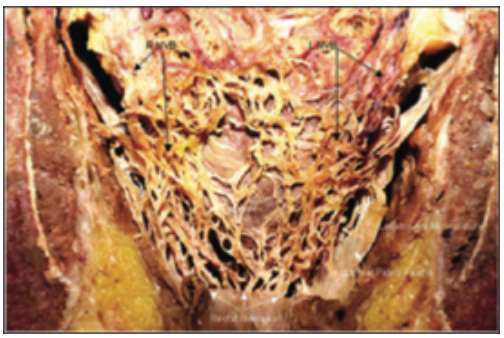

Figure 1.2: Neurovascular bundle, ventral view

Another significant structure is the dorsal vascular complex, which lies ventrally to the prostate and the urethral sphincter. The complex serves to drain blood from the penile veins [5]. The external urethral sphincter, which is found distal to the prostatic apex, serves to open and close the path of urine from the bladder to the penis [2].

The prostate is divided into 3 zones, Fig.1.3 :

- peripheral

- transition
- central

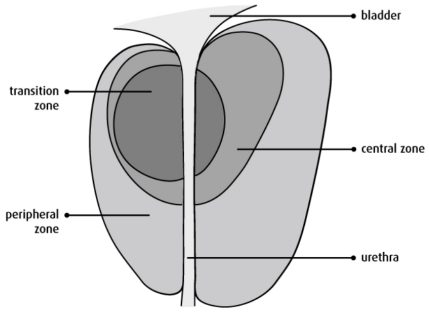

Figure 1.3: Prostate zones

The peripheral zone is the area of the prostate that is closest to the rectum. It can easily be felt by the doctor during a digital rectal examination (DRE). It is the largest zone of the prostate gland. The majority of prostate tumours (approximately 75%) are found in the peripheral zone [6].

The transition zone is the middle area of the prostate, between the peripheral and central zones. It surrounds the urethra as it passes through the prostate. This zone makes up about 20% of the prostate gland until the age of 40. As men age, the transition zone begins to enlarge, until it becomes the largest area of the prostate. This is called benign prostatic hyperplasia (BPH). When the transition zone enlarges, it pushes the peripheral zone of the prostate toward the rectum.

The central zone is in front of the transition zone. It is the part of the prostate that is farthest from the rectum. Because of this, prostate tumours in this zone cannot be felt by the doctor during a DRE.

The muscular tissue within the prostate is mainly smooth muscle. Anterior to the urethra, a layer of smooth muscle merges with the main

mass of muscle in the fibromuscular septa; this anchors the prostate in a stable position [1]. The consistency and the relatively fixed position of the prostate prove that palpation is ideal for this gland, FIg.1.5.

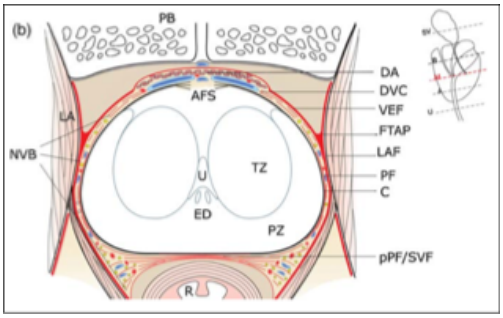

Figure 1.4: Schematic of axial section of prostate and periprostatic fascia at midprostate

The main function of the prostate is to produce the fluid portion of semen. The gland cells within the prostate produce a thin fluid rich in proteins and minerals that maintain and nourish sperm. This fluid is made continuously. The excess passes from the body in the urine. The prostate also plays a part in controlling the flow of urine. The urethra runs from the bladder, through the prostate, and out through the penis. The muscle fibres of the prostate are wrapped around the urethra and are under involuntary nervous system control. These fibres contract to slow and stop the flow of urine.

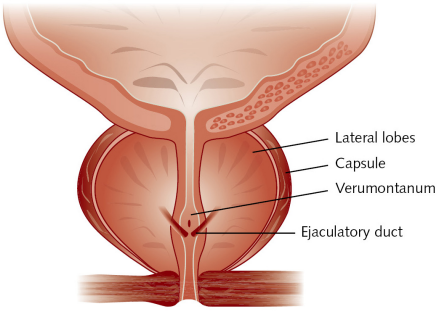

Figure 1.5: Prostate: ejaculatory duct to secret fluid that maintain and nourish sperm

1.2 Prostate cancer and clinical approaches to screening, diagnosis and treatment.

Prostate cancer is the second most frequently diagnosed cancer and the sixth leading cause of cancer death in males worldwide [6].

	Common Types of Cancer	Estimated New Cases 2014	Estimated Deaths 2014
1.	**Prostate Cancer**	**233,000**	**29,480**
2.	Breast Cancer (Female)	232,670	40,000
3.	Lung and Bronchus Cancer	224,210	159,260
4.	Colon and Rectum Cancer	136,830	50,310
5.	Melanoma of the Skin	76,100	9,710
6.	Bladder Cancer	74,690	15,580
7.	Non-Hodgkin Lymphoma	70,800	18,990
8.	Kidney and Renal Pelvis Cancer	63,920	13,860
9.	Thyroid Cancer	62,980	1,890
10.	Endometrial Cancer	52,630	8,590

Figure 1.6: Common Types of cancer in U.S

In 2011, there were an estimated 2,707,821 men living with prostate cancer in the United States, and approximately 15.3% of men will be diagnosed at some point during their lifetime. Furthermore, prostate cancer represents 14% of all new cancer cases domestically. An estimated 29,480 will die of prostate cancer in 2014 [7].

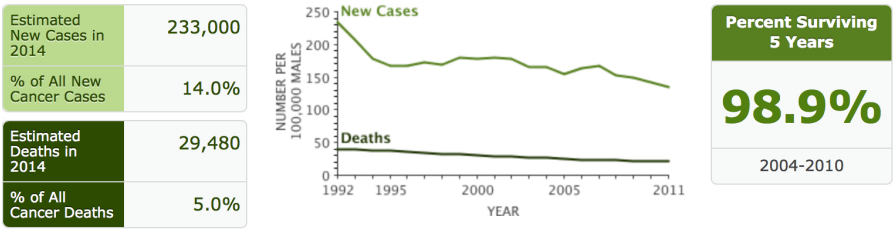

Figure 1.7: Percent survival rate of 5 years.

Although the 5-year survival rate for prostate cancer is very good at 98 %, one study found that up to 35% of those cases can metastasize to

locations such as bone and lung, making treatment much more difficult [7] [8]. This makes prostatectomy, the surgical removal of the prostate, a recommended treatment option for prostate cancer, especially when the cancer is at an early stage and is completely confined in the prostate [9].

Fig.1.8 shows the different stages of prostate cancer

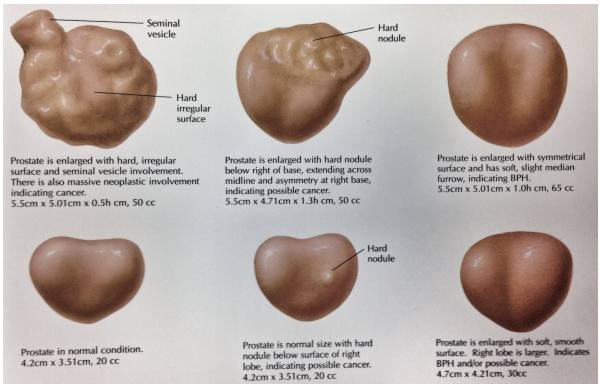

Figure 1.8: Stages of prostate cancer.

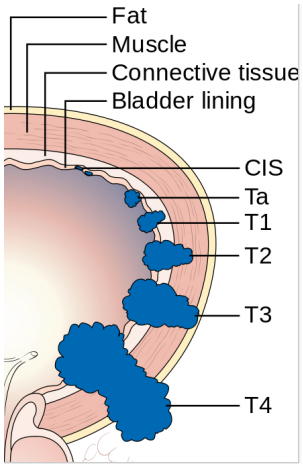

Figure 1.9: Diagram showing the T stages of bladder cancer that are the same in the prostate

Determining the stage is an important part in evaluating prostate cancer. The most common system is the four-stage TNM system (abbreviated from Tumor/Nodes/Metastases). Its components include the

size of the tumor, the number of involved lymph nodes, and the presence of any other metastases. In the TNM system, clinical T1 and T2 cancers are found only in the prostate, while T3 and T4 cancers have spread elsewhere

As aforementioned the consistency and the relatively fixed position of the prostate prove that palpation is ideal for this gland. Although other methods of detecting tumor tissue are available, they have proven to be inadequate in accurately localizing neoplastic tissue.

Transrectal ultrasound (TRUS), Fig.1.10. is the standard imaging modality for prostate biopsy and radiation. However, neoplastic tissue does not have a visually distinct appearance in ultrasound images [10]. The nonuniform appearance of malignant tissue in ultrasound images is partly explained by the morphologic diversity of prostate cancer. Not all tumor sites appear hypoechoic in ultrasound, which makes TRUS an unreliable and inaccurate method of localizing cancer tissue [11].

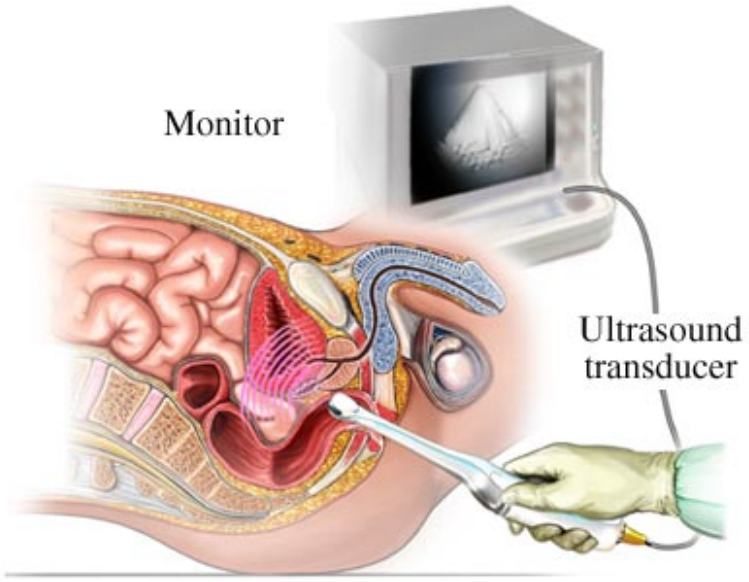

Figure 1.10: TRUS for localizing prostate cancer.

Screening for prostate cancer is done using two tests: the prostate-

specific antigen test and the digital rectal examination. The prostate-specific antigen (PSA) test measures the blood level of PSA, a protein that is produced by the prostate. The higher the PSA level, the more likely it is that prostate cancer exists [12]. In the digital rectal exam, the prostate is physically palpated, examining for abnormal enlargement or other signs of prostate cancer [13]. Tumoral masses are typically stiffer than healthy tissue by 70% [14] and can be recognized by tactile clues.

Thomas A. Krouskop et al. studied the mechanical behaviour of different prostate tissues (i.e fibrous tissue, connective tissue, tissue with benign prostatic hyperplasia (BPH) subject to compression loading. The results showed that the normal prostate tissue has a elastic modulus that is lower than the modulus of the prostate cancer and there is not significant difference between the modulus of the anterior and posterior part of the prostate. Fig.1.11 and 1.12

Prostate Tissue Type	Tissue Elastic Modulus (kPa)					
	2% precompression			4% precompression		
	Loading frequency (Hz)			Loading frequency (Hz)		
	0.1	1.0	4.0	0.1	1.0	4.0
Normal anterior (n = 32)	55 ± 14	62 ± 17	59 ± 19	60 ± 15	63 ± 18	63 ± 16
Normal posterior (n = 32)	62 ± 19	69 ± 17	65 ± 18	68 ± 14	70 ± 14	71 ± 11
BPH (n = 21)	38 ± 8	36 ± 9	38 ± 8	40 ± 12	36 ± 11	41 ± 13
Cancer (n = 28)	96 ± 19	100 ± 20	99 ± 18	230 ± 34	221 ± 32	241 ± 28

Figure 1.11: Tissue elastic moduli in the normal and abnormal prostate tissues at different frequencies and precompression strain level

Diagnosis of prostate cancer is based on two criteria: the prostate-specific antigen test and the Gleason score [15]. In addition to the previously mentioned PSA test, the Gleason score is a system of grading prostate cancer based on how a biopsy sample looks under a microscope. Scores range from 2 to 10 and indicate how likely it is that a tumor will spread [16]. A PSA level of less that 10 ng/mL and a Gleason score of 6

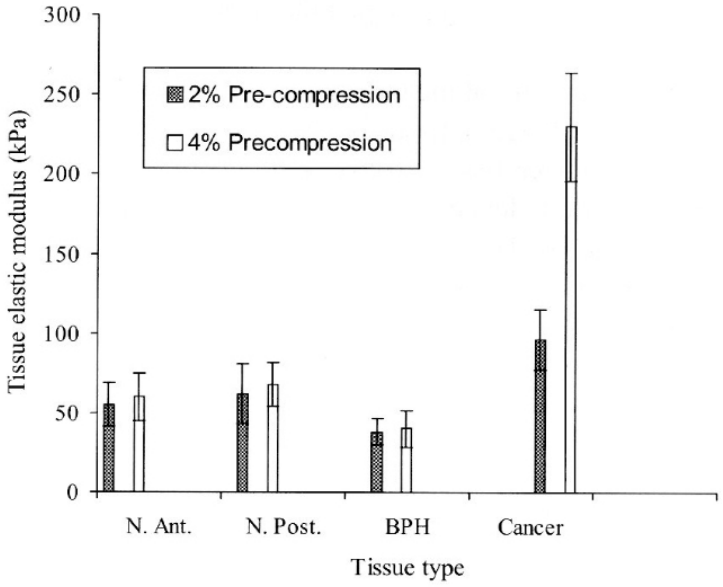

Figure 1.12: Summary of the leasetic modulus of the different combonents of the prostate tissue obtained at a loading frequency of 0.1 Hz and for recompression strain levels of 2% and 4%

or less is classified as low-risk prostate cancer [15]. The American Urological Association defines high-risk prostate cancer as a PSA greater than 20 ng/mL and a Gleason score of 8-10 [17].

1.3 Surgical Procedures

Open radical prostatectomy has been considered the gold standard for the surgical treatment of localized prostate cancer. However, due to its relevant rate of complications, high loss of blood, big scars, long rehabilitation periods, has been largely replaced by a minimally invasive approach, such as laparoscopic or robotically assisted surgery. Currently, minimally invasive surgery (MIS) has become the standard of care for prostatectomy at many institutions worldwide [18].

Due to its effects of less postoperative pain, smaller incision scars, and

shorter hospitalization time, MIS is currently a well-established technique, with more than two million procedures performed in the United States annually [19]. Compared with the traditional open radical prostatectomy, minimally invasive prostatectomy is associated with decreased operative blood loss and decreased risk of transfusion [20].

Robotics have recently been introduced to address motion constraints in MIS, rapidly becoming a popular, widely accepted clinical practice. Today, approximately 60% of radical prostatectomies performed in the United States were done using robotic assistance [18]. Compared with laparoscopic prostatectomy, it was found that the robotic approach resulted in a significant shorter length of hospital stay and improved 12 months continence and potency rates [22].

A common method of treatment with robotics is surgical removal, more specifically robotic-assisted laparoscopic prostatectomy. Placement of the ports for the laparoscopic trocars is vital to provide the maximal amount of working flexibility. There are six incisions in total, Fig.1.13.

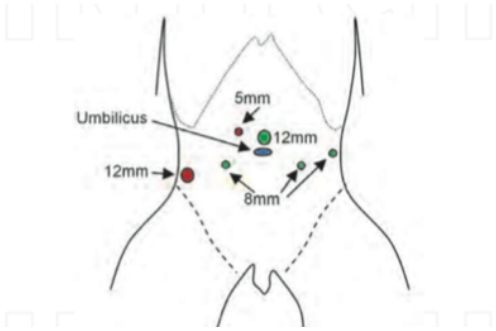

Figure 1.13: Schematic of port placement for robotic prostatectomy

A 12 mm trocar is placed either superior to the umbilicus or to either side of the umbilicus for the endoscopic camera [25]. Two 8 mm trocars are placed 10-12 cm to either side of the midline, a fingerbreadth inferior to the level of the umbilicus for laparoscopic tools. A 10-12 mm trocar

is inserted just above the right anterior superior iliac spine for retraction and passage of sutures. An 8 mm is placed opposite to the 10-12 mm trocar, on the patient′s left side. Finally, 5 mm port is placed midway and slightly inferior to the umbilicus and the right robotic port.

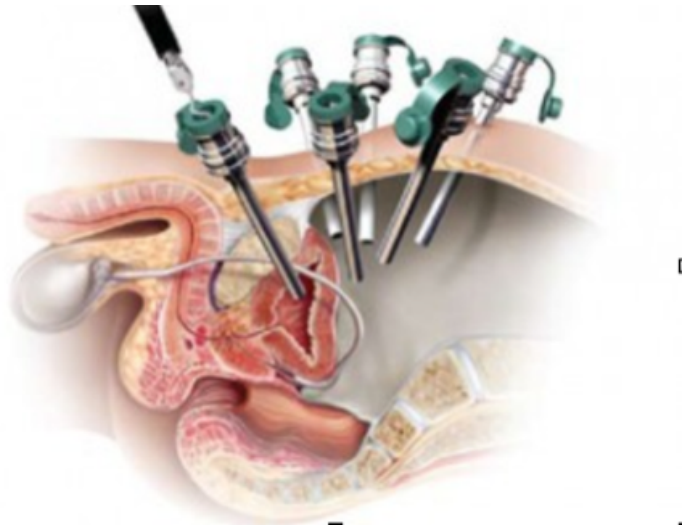

Figure 1.14: Sagittal view of laparoscopic prostatectomy. Abdominal space is insufflated and six trocars are seen

After port placement the patient is placed in a Trendelenburg position, which is described as a supine position with the head declined [26]. The angle of decline can vary. The legs are supported and abducted to allow robotic access to the lower abdomen, Fig.1.15.

The prostatectomy procedure itself is relatively simple. The main objectives are to ligate the vascular connections of the prostate, remove the prostate, and join the bladder neck to the urethra, re-establishing the integrity of the route of the urinary pathway.

First, the peritoneum is incised and the bladder is released from the ventral wall of the abdomen. The periprostatic fat is removed, and the endopelvic fascia is preparated and incised, allowing better exposure of the prostatic borders. The dorsal vascular complex s exposed and ligated,

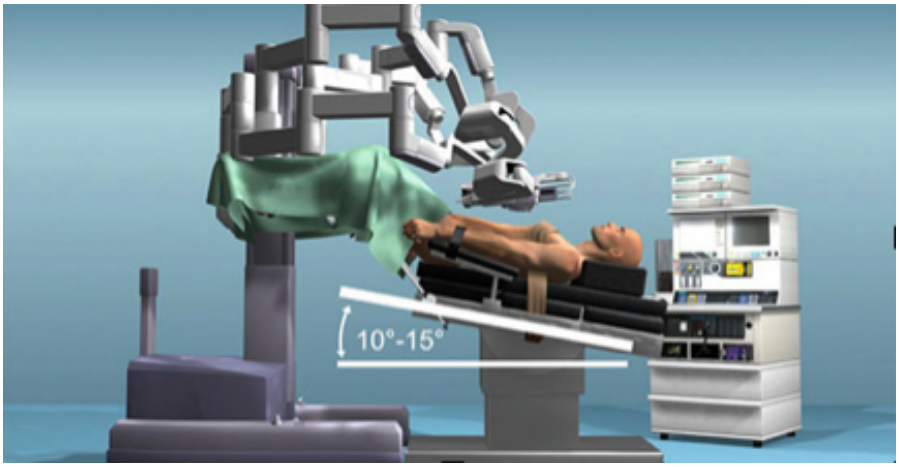

Figure 1.15: Side view of patient position during robotic-assisted laparoscopic prostatectomy: Trendelenburg position

preventing blood loss when the prostate is removed. The vas deferens and seminal vesicular vessels are clipped.

The neurovascular structures, which are located on the lateral surfaces of the gland, are separated from the prostate. Depending on the risk level of the prostatic cancer, more of the neurovascular bundles are preserved. In low risk patients the neurovascular bundle can be prepared close to the prostate in an intrafascial approach. This preserves the bundle, thus sparing the function of continence and potency. In medium risk patients, the preparation can be performed in an interfascial way by leaving the small artery that travels laterodorsally on the prostate on the specimen. When an extraprostatic lesion is visible, the patient is high risk, and the neurovascular bundle is widely resected, leaving little of the nervous function [25].

The urethra is exposed inferior to the prostate and incised. The prostate, and lymph nodes if needed, is then removed from the patient. Finally, anastomosis is performed, joining the bladder to the urethra, Fig.1.16.

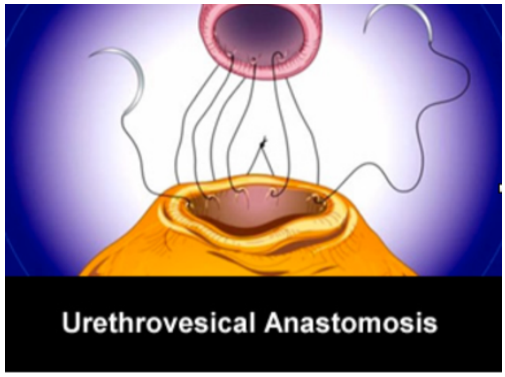

Figure 1.16: Illustration of prostatectomy anastomosis, the joining of the bladder neck (bottom) to the distal urethra (top)

This is the result before and after a prostatectomy is shown in Fig.1.18

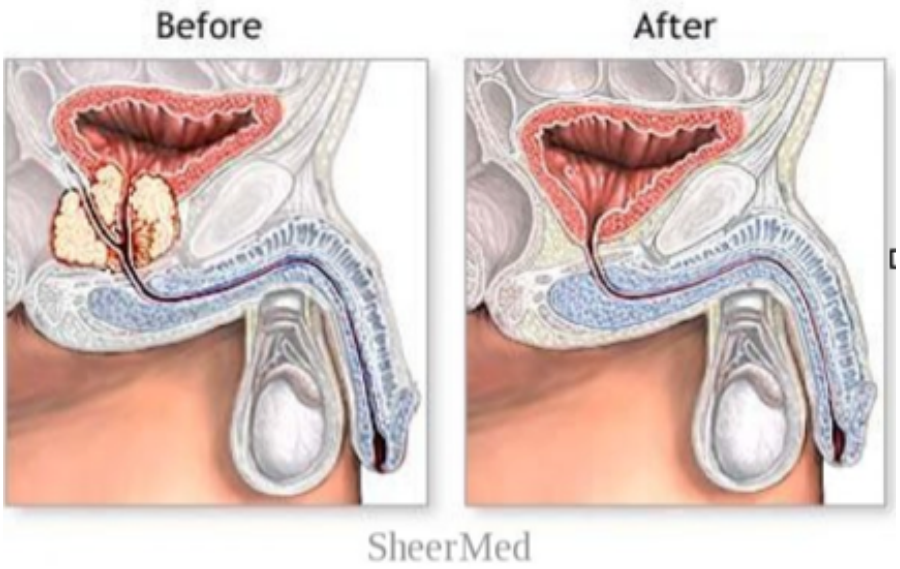

Figure 1.17: Illustration of prostatectomy, before and after.

1.3.1 Limitation/Open Issues

Despite their clear benefits, both MIS and robotic MIS prevent the surgeon from directly manipulating tissues and organs as is done in open

surgery [27].

In particular, laparoscopic instruments used in MIS severely compromise any haptic cues because of friction against the surgical port (i.e., trocar) and the fulcrum effect at the insertion point [28]. The situation is worsened for commercially available robotic MIS platforms, where zero haptic force feedback is available, since the surgical instruments are teleoperated from a remote console.

A significant issue concerning prostatectomy is the practice of nerve sparing surgery. It is known that the neurovascular bundles that lie to either side of the prostate innervate important genitourinary functions such as erection and detrussor control. Although prostatectomy is effective at eradicating the cancer, the side effects of urinary incontinence and erectile dysfunction can severely affect quality of life for post-operative patients [29].

Willis et al. found that while urinary continence was retained in 92.5% of prostatectomy patients 12 months, post-surgery, sexual function was retained in only 73.7% of prostatectomy patients. These data coupled with the high incidence of prostate cancer, result in thousands that lose sexual potency through the prostatectomy procedure [2].

Visual options such as transrectal ultrasound are occasionally used to guide operations such as biopsy and nerve-sparing prostatecomy with some success, but there is no current option to localize tumor prior or during surgery [30].

Therefore, in MIS and robotic MIS the surgeon has minimal, or no, chance to leverage tactile and kinesthetic sensations in exploring non-visible prostate features to detect locations of the tumor or to prevent neurovascular nerves damage or unnecessary tissue resection. Restoring

tactile sensations would be crucial to define prostatic tumor margins, thus guiding a complete resection without sacrificing excess normal tissue and preserving the neurovascular bundles more efficiently.

To address these constraints, we propose a novel tissue palpation approach, where a soft robotic skin is deployed through a standard trocar, docked on the prostate by magnetic coupling, and operated without requiring surgical assistance to create a mechanical stiffness map of the prostate.

Given the novelty of the approach, this work aims to introduce the concept and the principle of operation, and then focuses on the pressure sensing submodule of the robotic skin. If successful, the proposed approach can reduce the number of patients that suffer from post-operational sexual impotence, therefore improving their quality of life.

1.4 Palpation: State of Art

Restoring haptic sensations in MIS and robotic MIS has been an active research topic for more than two decades [31], [32], with one of the first systems used in a human dating back to 1994 [33]. A relevant number of MIS instruments with force and/or tactile sensors have been developed to acquire in vivo data for tissue modeling and simulation [34] [35], to improve the outcomes of the surgical procedure preventing excessive forces from being applied to the tissues [36], [37] or to create stiffness distribution map by palpation [38], [39], [40] [41].

Hongbin Liu et al. described a novel approach for the localization of tissue abnormalities during minimally invasive surgery using a force-sensitive wheeled probe. The concept is to fuse the kinaesthetic information from the wheel/tissue rolling interaction into a pseudocolor rolling

mechanical image (RMI) to visualize the spatial variation of stiffness within the internal tissue structure [43].

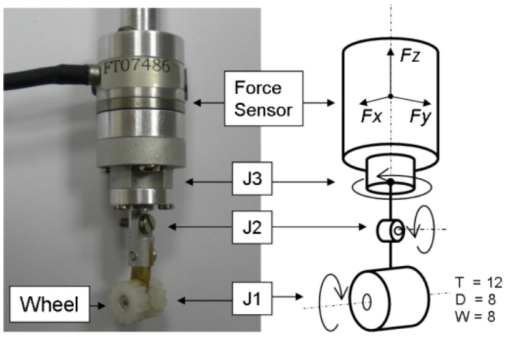

Figure 1.18: The force-sensitive probe with a grooved wheel end-effector; The wheel has 12 teeth (T) along its circumference, is 8 mm in diameter (D) and 8 mm in width (W).

When compared to multiple discrete uni-axial indentations, the continuous measurement approach of RMI is shown to be more sensitive and facilitates coverage of a large area in a short period of time

Beccani et al. developed a wireless palpation probe for lump detections. The wireless palpation probe (WPP) is a cylindrical device (15 mm in diameter, 60 mm in length) that can be deployed through a trocar incision and directly controlled by the surgeon to create a volumetric stiffness distribution map of the region of interest [42].

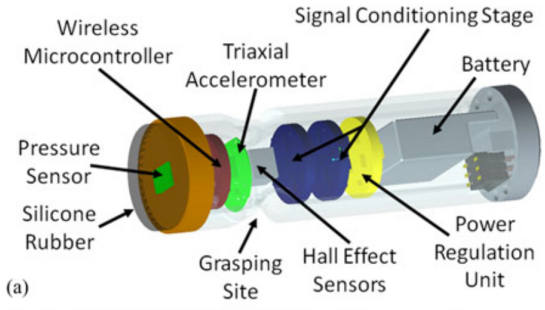

Figure 1.19: WPD: schematic view.

The WPP was assessed on the benchtop in detecting the local stiffness

of two different silicone tissue simulators (elastic modulus ranging from 45 to 220 kPa), showing a maximum relative error below 5%.

1.5 Aim of the Work

In order to investigate the feasibility of the proposed approach and present a first Soft Robotic Skin (SRS) device the aim of this work is:

Develop, Test and Characterize the Sensing Module of the SRS for identification of prostate cancer.

Chapter 2

Material and Methods

2.1 Principle of Operation

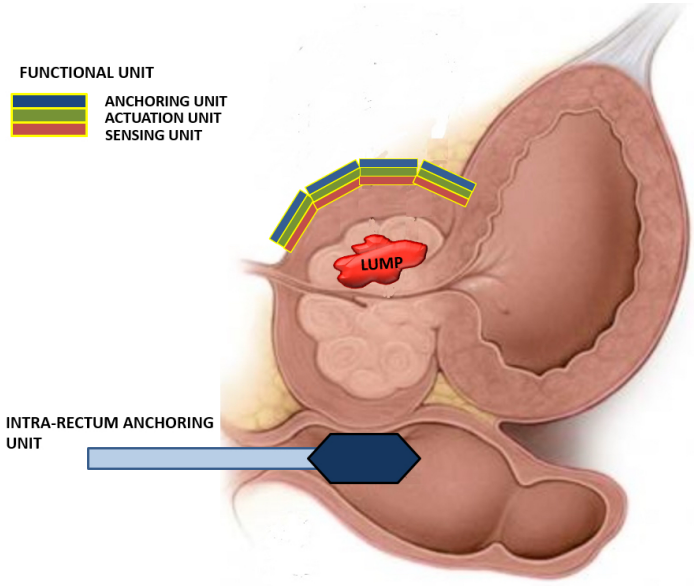

Figure 2.1: Principle of operations for tissue palpation using a Soft Robotic Skin (SRS)

Referring to Fig.2.1, The system is composed of different parts:

- **an intra-operative Soft Robotic Skin** that is mechanically actuated by air and is responsible of palpating the prostate.

- **an intra-rectum anchoring unit** for docking the skin around the prostate during the palpation procedure.
- **a workstation** to operate the skin for both actuation and sensing.

The SRS can be introduced into the abdominal cavity through a standard trocar or through the incision before entering the trocar, and positioned on the target using a laparoscopic grasper. The surgeon moves the device until magnetic coupling with the intra-rectum unit is achieved and the skin is stable on the surface of the prostate. The stiffness map can then be obtained by inflating each air chamber sequentially by a constant (known) pressure and acquiring the tactile response at the interface between the robotic skin and the tissue. In order to generate kinesthetic data, the indentation depth and the pressure applied on the tissue must be known at any given time.

Three functional sub-modules are present in the SRS (Fig.2.2): the sensing module, the actuation module, and the anchoring module.

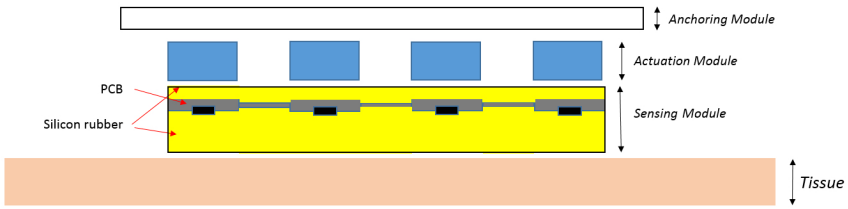

Figure 2.2: Soft robotic skin submodules: Sensing, Actuation and Anchoring

- The **Sensing module** (Fig2.3) is composed of a flexible PCB with barometric pressure sensors soldered on the top layer. Both the sensors and PCB are embedded in a silicone rubber to obtain a tactile array.

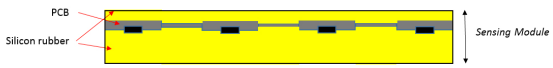

Figure 2.3: Sensing module

- The **Actuation module** is composed by air chambers embedded in silicone rubber that are inflated when palpation is performed, the walls of the air chambers are made by different rubber with different stiffness so that the displacement due to the increase of pressure happens only in one direction. The actuation is controlled externally by small valves and air pumps.

- The **Anchoring module** is composed of magnets and a layer of kapton. The magnets are embedded in the silicon rubber and positioned along the edges of the skin. These magnets couple with the ones in the intra-rectum anchoring unit with the goal of keeping the skin in contact with the prostate. A thick layer of katpon is used to keep the device in contact with the prostate during inflation of the air chambers.

The intra-rectum anchoring unit embeds a series of magnets designed to couple with the robotic skin at a distance of 3 cm without generating excessive pinching force to arm the tissue in between.

Since the skin is made by taxels that perform the same function, it is possible to describe the p working principle of the single functional unit (shown in Fig.2.4) and then extend the same principle to the skin.

Considering the functional unit oriented as in Fig.2.5, we studied the indentation of a tissue sample along the vertical direction by cyclically inflating the chamber behind the sensing component. The chamber has been designed using a model of a cylinder tube having different mechanical

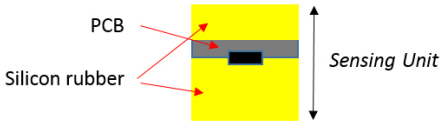

Figure 2.4: Sensing unit

properties, the material around is composed of different materials that present variable thicknesses. It must be ensured that the only side of the chamber that will manifest a displacement is the sensing one so it is possible to generate a pure vertical motion of the sensor.

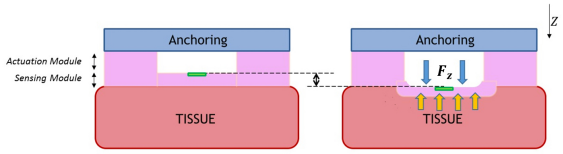

Figure 2.5: SRS against tissue: Principle of operation.

The pressure exerted on the tissue is provided by the force induced in the Z direction after inflating the air chamber, F_z, and the area of the functional unit face in contact with the tissue. At the equilibrium, the intensity of F_z can be controlled by the external control unit and can be considered constant.

For indentation depths that are less than 10% of the organ thickness, it is possible to assume the tissue as linear elastic [43]. A volumetric stiffness map is usually created by estimating the local tissue stiffness $E(t)$ through the measurement of the indentation depth $\delta(t)$ and the tissue reaction pressure $P(t)$ at different positions r on the organ surface

$$E(t) = P(t)/\delta(t) \tag{2.1}$$

Alternatively, the local tissue stiffness can be estimated by imposing a known pressure P_{in} to the deformable element, defined as the pressure sensor embedded in silicone and the tissue, and reading the pressure data P_{out} measured by the sensor. This method, schematically represented in Fig.2.6, allows us to reconstruct a local stiffness map without necessarily knowing the indentation depth during palpation.

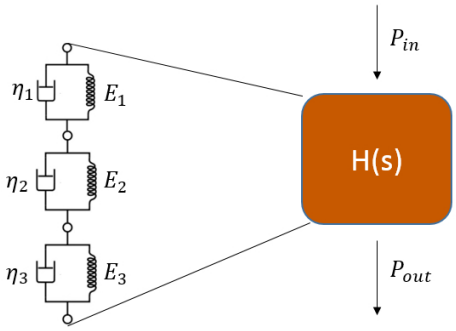

Figure 2.6: Transfer function of three components of the Kelvin-Voight model

The transfer function $H(s)$ was than validated experimentally thus allowing to map, for each sensor, the P_{in} applied through the air chamber with the correspondent P_{out}.

So for each instant of time it is possible to obtain a $r \times c$ matrix of $P_{out}(r, c)$ measured by the sensors, where r and c are the number of sensors on the row and column respectively and compare it with an $r \times c$ matrix of $P_{out(model)}(r, c)$ estimated by the model from the input P_{in}.

The result is a pseudo stiffness matrix $E = \frac{P_{out}(r,c)}{P_{out(model)}(r,c)}[\frac{Pa}{mm^2}]$ where every results > 1 means that a higher stiffness respect to the value predicted from the model is detected.

In this pilot study, we restricted the investigation to the sensing unit as a first step toward proving the feasibility of the proposed approach.

2.2 Dynamic Model

Viscoelastic materials, such as amorphous polymers, semicrystalline polymers, and biopolymers, can be modeled in order to determine their stress or strain interactions as well as their temporal dependencies. These models, which include the Maxwell model, the Kelvin-Voigt model, and the Standard Linear Solid Model, are used to predict a material response under different loading conditions. Viscoelastic behavior has elastic and viscous components modeled as linear combinations of springs and dashpots, respectively.

Each model differs in the arrangement of these elements, and all of these viscoelastic models can be equivalently modeled as electrical circuits. In an equivalent electrical circuit, stress is represented by current, and strain rate by voltage. The elastic modulus of a spring is analogous to a circuit capacitance (it stores energy) and the viscosity of a dashpot to a circuit resistance (it dissipates energy).

It is known from literature that solid composite viscoelastic material (material constituted of different layers that are in contact and have different mechanical characteristic) can be modeled by using a Kelvin-Voight model [43]. The Kelvin-Voigt model consists of a Newtonian damper and Hookean elastic spring connected in parallel, as shown in the Fig.2.7. It is used to explain the creep behaviour of polymers.

This model represents a solid undergoing reversible, viscoelastic strain. Upon application of a constant stress, the material deforms at a decreasing rate, asymptotically approaching the steady-state strain. When the stress

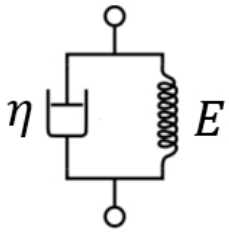

Figure 2.7: Kelvin-Voight Model for a single viscoelastic element.

is released, the material gradually relaxes to its undeformed state.

At constant stress (creep), the model is quite realistic as it predicts strain to tend to σ/ϵ as time continues to infinity. Similar to the Maxwell model, the Kelvin-Voigt model also has limitations. The model is extremely good with modelling creep in materials, but with regards to relaxation the model is much less accurate.

Since the two components of the model are arranged in parallel, the strains in each component are identical:

$$\epsilon = \epsilon_1 = \epsilon_2 \tag{2.2}$$

Similarly, the total stress will be the sum of the stress in each component:

$$\sigma = \sigma_1 + \sigma_2 \tag{2.3}$$

From these equations we get that in a Kelvin-Voigt material, stress σ, strain ϵ and their rates of change with respect to time t are governed by equations of the form:

$$\sigma(t) = E\epsilon(t) + \eta\frac{d\epsilon(t)}{dt} \tag{2.4}$$

where E is a modulus of elasticity and η is the viscosity.

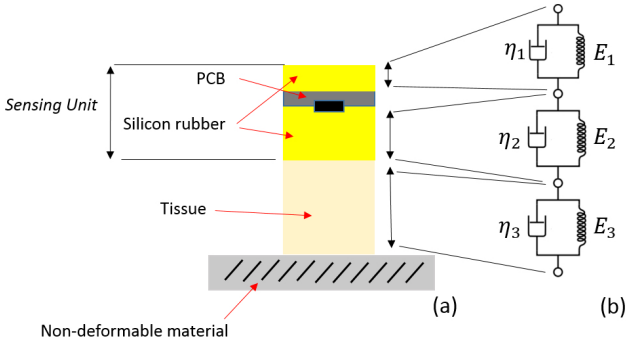

Figure 2.8: Kelvin-Voight Model composed by 3 components in series.

Our system Fig.2.8 can be model by three Kelvin-Voight components in series, the first one represents the thickness of rubber on the back of the PCB board, the second is the layer in between tissue and silicon and the third represents the tissue.

The electrical equivalent of the system is shown in Fig.2.9

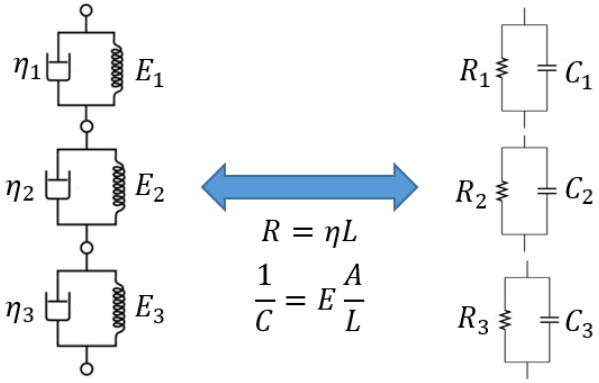

Figure 2.9: Electrical equivalent of Kelvin-Voight mechanical model.

Where

$$V(t) = \frac{1}{C}Q(t) + R\frac{dQ(t)}{dt} \tag{2.5}$$

where $\frac{1}{C} = E\frac{A}{L}$ and $R = \eta L$. A and L are the area and the thickness of the component.

The transfer function of the system can be obtained by calculating the ratio V_{out}/V_{in} throught the Laplace domain. The resulting transfer function is showed in equation 2.6

$$H(s) = \frac{as^2 + bs + c}{ds^2 + es + f} \tag{2.6}$$

where

$a = R_2\tau_1\tau_3 + R_3\tau_1\tau_2$

$b = R_2\tau_1 + R_3\tau_1 + R_3\tau_2 + R2\tau_3$

$c = R_2 + R_3$

$d = \tau_1\tau_3R_2 + R_3\tau_2\tau_1 + R_1\tau_3\tau_2$

$e = R_2\tau_1 + R_3\tau_1 + R_2\tau_3 + R_3\tau_2 + R_1\tau_3 + R_1\tau_2$

$f = R_2 + R_3 + R_1$

The Bode plot of the transfer function is showed in fig 2.10.

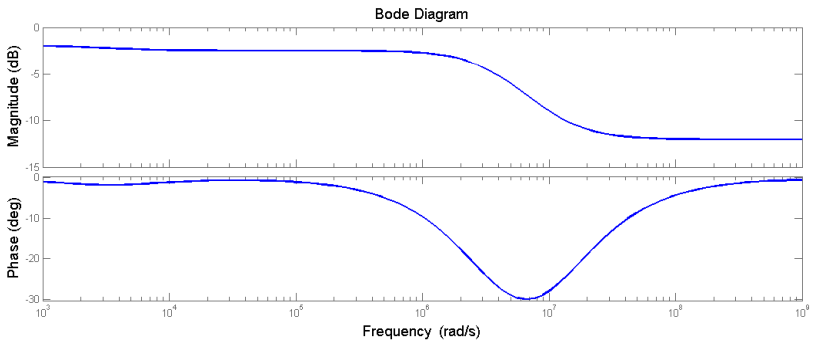

Figure 2.10: Bode Plot

2.3 Soft robotic skin fabrication

2.3.1 Sensing Unit

The aim of the sensing unit is to evaluate the difference of stiffness of the tissue. As aforementioned, the area in which the probability of finding a tumor is higher is the peripheral zone (approx 75%) and the lumps that were found in this zone are usually 4 times stiffer than the surrounding area [14].

In addition to the previous medical requirements that have been discussed in chapter 1.2, the design of the sensing unit has to take in consideration also this preliminary mechanical and electrical requirements:

- The device needs to be able to bend around the organ without breaking
- The dimension of the whole sensing device cannot exceed the dimension of the prostate
- The device needs to be able to recognize tumors in all the prostate with a costant spatial resolution, avoiding black spots.
- The sensors have to be small enough to be soldered on a flexible skeleton.
- The thickness of the silicone needs to be small enough to allow the device to bend and be inserted during a surgical operation
- The speed of acquisition of the whole sensing array has to be fast enough to allow real-time stream of the data.

Despite a relevant number of tactile sensors have been reported in the literature thus far, a standardized way to design them has not been

established yet [45] [46]. Inexpensive pressure sensors (e.g., Flexi- Force, Tekscan Inc., South Boston) often provide limited accuracy and significant hysteresis. In addition, the engineering effort required to integrate these sensors into arrays (including wiring, amplification, analog multiplexing, and analog-to-digital conversion) usually overwhelms the transducer cost. Commercial tactile array sensors avoid the need to master fabrication technologies and integrate sensors into arrays, but they are typically costly and fragile and cover only a limited area [47] [48].

The sensing unit was chosen to be the MPL115A2 (barometric pressure sensor, Freescale Semiconductors, Austin, TX, USA). Recently, several studies proposed to use this element as core for tactile probes by embedding it in a silicone rubber whose thickness varies depending on the application [49] [51].

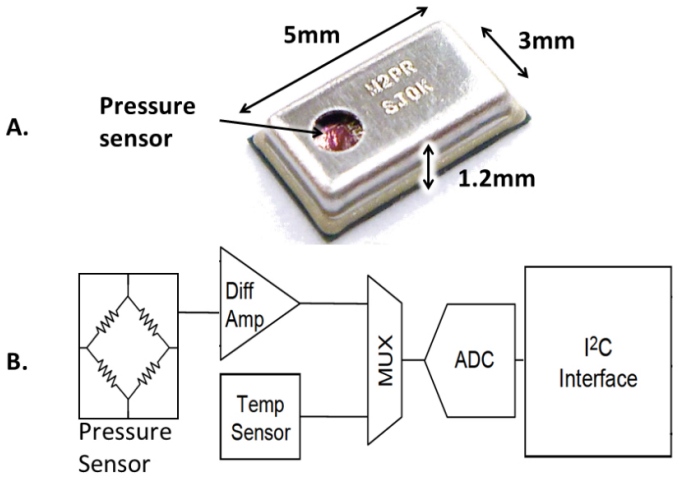

Figure 2.11: MPL115A2 sensor from Freescale Semiconductor, and the block diagram of the device

Beccani et al, caratterized the head (made by the MPL115A2 embedded in silicone rubber) of the wireless tissue palpation device for detecting lump inside the tissue. In this work, different parameters for the sensing

element were investigated. The results showed a tumor detection rate over 90%, independent of the head diameter, when an indentation depth of 5 mm is applied on the tissue simulator [51] .

Leif P. Jentoft et al, studied the first prototype of flexible and stretchable tactile array for many applications that require to measure forces on deformable objects. They proposed a sensor array created with barometers and flexible PCB that delivers high sensitivity on a flexible, stretchable package using commercial off-the-shelf (COTS) components: MEMS barometers and flexible PCB. The array then is demonstrated on the surface of a jamming gripper, where it provides the ability to sense grasping events and detect object shape [52] .

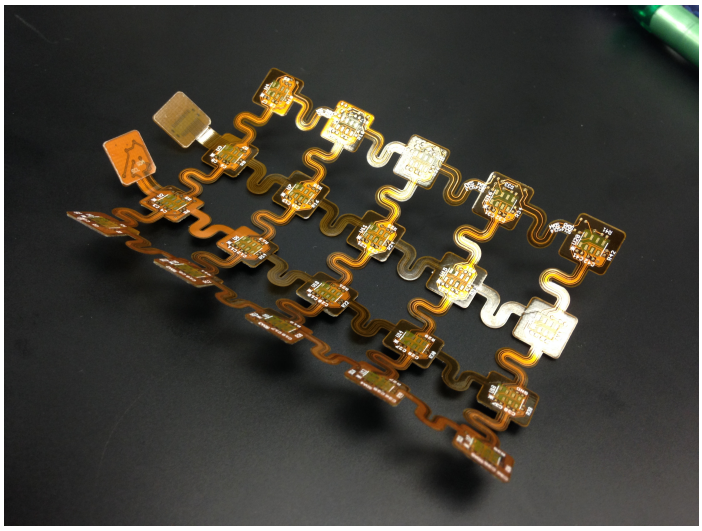

Figure 2.12: Flexible circuit prototype.

Based on all the previous studies and the medical considerations, the prototype, rapresented in (Fig.2.12) can be divided in taxels, each taxel have either the function of sensing or electrical connection. All the taxels together are connected by flexible circuit.

A. Taxel

The sensing taxel (Fig.2.14) of a dimension of 9x9 mm is composed

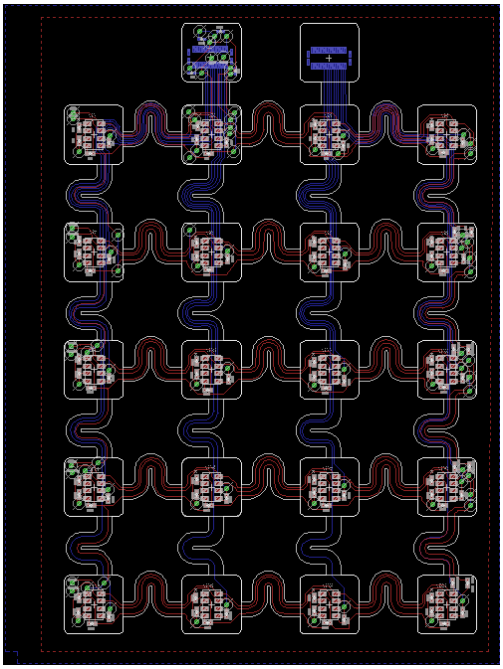

Figure 2.13: Eagle schematic of the prototype showed in Fig 2.12.

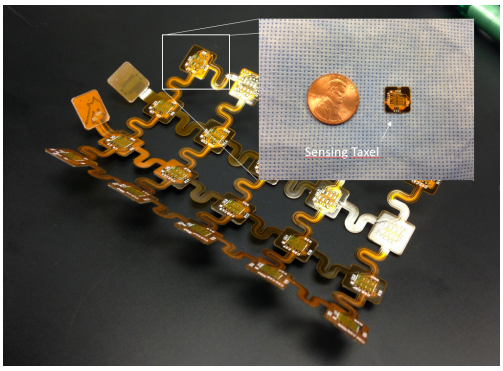

Figure 2.14: Sensing Taxel.

by a barometric pressure sensor mounted on a rigid PCB. To avoid that the taxel bend when an external force is applied a stiffener was mounted on the bottom layer.

Barometric sensor chips were originally developed for consumer products, such as desktop weather stations and global positioning systems, where altimeters can improve vertical positioning accuracy [8]. As such, these sensors have a small footprint and low power consumption, and they

are mass-produced at low cost. These sensors have an air pressure range of 50-115 kPa with a resolution of 0.15 kPa. This sensor also has a relatively large ventilation hole (1-mm diameter) directly above the pressure sensor.

The MPL115A2 can be embedded in soft silicone rubber to create a tactile sensor. Once the sensor is embedded it demonstrate an excellent linearity ($< 1\%$ typical), low noise, high sensitivity ($< 0,01$ N) and large bandwidth ($>$ 100Hz). These sensors could be easily addressed by an external circuit that allows multiple sensors to communicate on the same bus at over 100 Hz per sensor element [51] .

The process to convert the MPL115A2 chip into tactile sensors requires two steps:

- First, the sensor must be covered with rubber. This process leaves an air bubble inside the sensor providing very low sensitivity. This aspect was addressed by vacuum degassing the sensor unit in uncured rubber (DragonSkin10 Slow, Smooth-On, Inc., Easton PA) at roughly -740mm Hg (gauge) (refer to section degassing). This draws the rubber inside the metal case of the sensor before it cures to provide a direct force transmission from the rubber surface to the diaphragm of the sensor.

- Second, the MEMS barometers used for this design use I2C communication protocol with fixed address, and therefore requires additional circuitry when embedded into an array. To address this aspect, sensor should additionally be connected to a dedicated chip-select wire controlled by a micro-controller. This would make it possible to activate one sensor at a time for data sampling.

B. Wiring

To interconnect the array of sensors it was required to have wires that are flexible, stretchable and connecting at least four signals. One approach is to leverage flexible circuits. To enable them to stretch, several approaches have been studied including meandering [53], [54], micro patterning [55], and crinkling [56]. The meandering approach was chosen for the current work as it offers a significant elongation respect to the straight wire, and it is well suited for our bidimensional manufacturing techniques. Fig.2.15

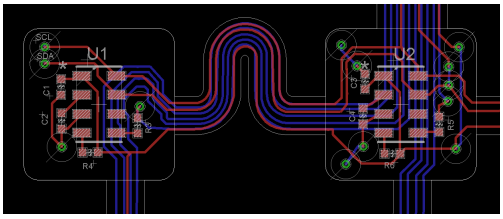

Figure 2.15: Wiring between two sensors: The meandering approach was chosen to ensure elongation to the array.

C. Array structure and PCB manufacturing

To interconnect the array of sensors, five signals must be brought to each sensor (V+, Ground, I2C data, I2C clock and Chip select). Since it is desirable to have just two connectors on the top of the surface the number of wires that go through each wire change along the structure. A two layer PCB was designed using Eagle. Referring to Fig.2.16 the chip select of each sensor was traced on the bottom layer and instead V+, ground and I2C bus were traced on the top layer. To ensure that the sensing module continues working even if one sensor of the line is broken, the I2C bus of each line was separated by the other lines and an external VIA for each I2C data and I2C clock was than inserted on each first taxel of the rows.

Referring to [52] , To assemble the sensor units and wires into an array,

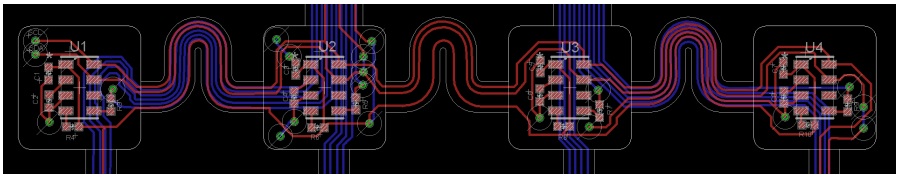

Figure 2.16: Array structure: Four wires are routed through the top Layer (red) : V+, ground, I2C data and I2C clock. The chip select of each sensor is routed on the bottom layer (blue).

several trade-offs are important to choose an appropriate size. First, there is a trade-off between array size and likelihood of failure. For an n-element array where each element has a failure rate of x, the failure rate of x the entire array will be x^n - this means a 40-element array of sensors with a 1% individual failure rate has a 33% chance of failure. Thus, for large arrays it is important to use either extremely reliable units, or to make it possible to replace individual units if they fail during manufacture or use.

Second, if the taxels are not themselves flexible, there is a trade-off between sensor density and the flexibility/stretchability of the array. More density is advantageous from a sensing standpoint, whereas more flexibility can be important to the end application (which ultimately dictates the proper trade-off between the two).

One way to resolve this is to look at the resolution required to avoid missing the object in deadzones (the spacing must be tighter than the size of the tumor) and to avoid other artifacts from tactile aliasing. Since this is a pilot study for what concern the tumor localization using a sensitive skin we started from a taxel spacing of 20mm and a 4x5 array.

The flexible PCB was fabricated with the layout reported in Fig.2.17 with the following guidelines

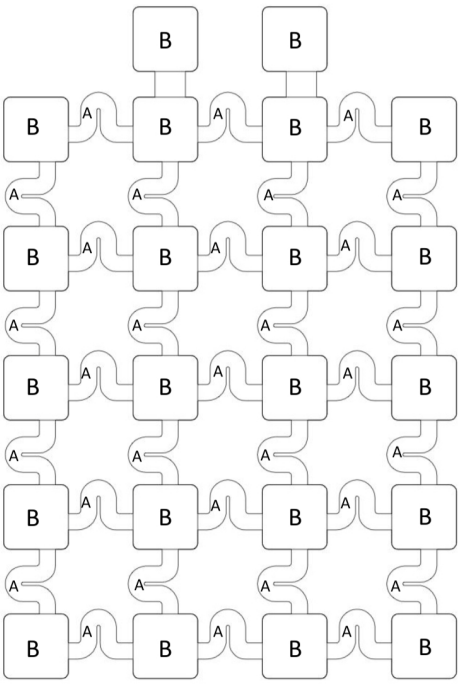

Figure 2.17: Fabrication guidelines: Regions A are without any stiffener applied, a final thickness of .15 mm was chosen to keep bending angles smaller. Regions B are areas where sensors and connettors are going to be soldered, The final thickness of .5 mm was chosen and a stiffner to match this height was applied

2.3.2 Silicone Molding and Degassing procedure

The second issue requiring special attention is the casting of the sensors in rubber. Rubber forms a robust and compliant contact surface for grasping and manipulation and serves to communicate surface contact pressure within the layer of rubber to the ventilation hole, and, thus, to the MEMS transducer. Encapsulation of the array can be readily accomplished by suspending the circuit board with mounted sensors in a mold and pouring in liquid polymer, which then cures to form the elastomer contact surface.

When molding is performed at atmospheric pressure, however, air is trapped within the sensor chip inside the ventilation hole. This results in

low sensitivity because the surface pressure produces only small changes in the volume of the trapped air below the ventilation hole.

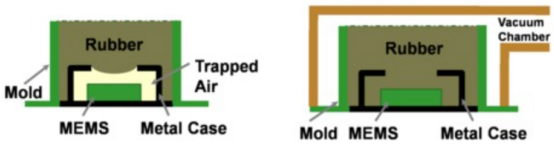

Figure 2.18: Degassing procedures: a) rubber does not fill the sensor area, b) degassing removes air bubbles, and the rubber fills the sensor

One solution is to remove the top of the sensor metal case so that the rubber directly encapsulates the MEMS pressure transducer. This improves sensitivity but requires nonstandard chip-handling techniques. This procedure also exposes fragile components, such as bond wires, that can break when large forces are applied to the rubber surface. A more successful approach is vacuum degassing. The mold is placed in a vacuum chamber (e.g., a standard laboratory bell jar) immediately after the rubber is poured, and the air is removed with a vacuum pump. This removes the air from inside the sensors, allowing the rubber to enter the case through the ventilation hole.

The fabrication procedure can be separated in 5 parts:

- First: the silicone was poured in a small container and stirred well for 5 minute, and at the end of the of the procedure a homogeneous viscous material is obtained

- Second: the mixture was degassed in the vacuum gauge following tree cycles in which the pressure was gradually raised up to a value of approx -740mm Hg and kept constant for 5 minute. Then the pressure value was gradually brought back to atmospheric.

- Third: the mixture was poured in the mold to create a thin layer of a thickness of 1mm (Fig.2.19) that represent the back of the sensing

unit. To achieve that, a plastic mold was fabricated by rapid prototyping (OBJET 30, Objet Geometries Ltd, Billerica, MA, USA). Then the part was left to solidify for 1 day.

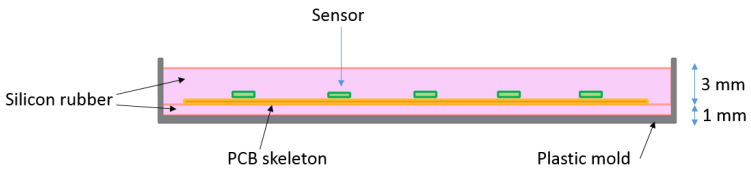

Figure 2.19: Schematic of the molding procedure, the rubber was poured in two steps: before the thin layer (1 mm) on the bottom of the PCB and then the top layer (3 mm)

- Fourth: the flexible skeleton was then lean on the top with sensors oriented to the top and the step 1 and 2 was made again. Then a layer af 3 mm was poured on top covering sensors and flexible PCB, and the part was then left to solidify for 1 day. The rubber thickness of 3 mm creates a 1.3 mm layer of rubber above the sensor. Fig.2.20

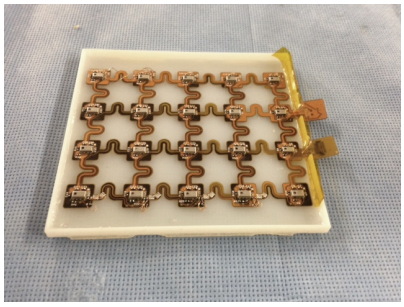

Figure 2.20: The PCB with all the sensors on a 1 mm of rubber before the other layer was poured.

- Fifth: the flexible skin was extruded from the plastic mold and all the electrical tests were made.

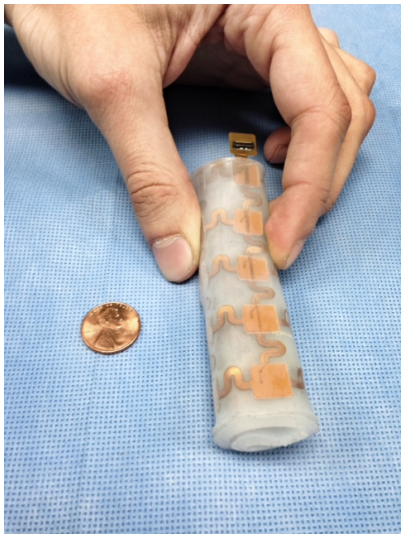

Figure 2.21: The resulted skin extruded from the plastic mold.

The fabrication part was really important and delicate. In the steps illustrated before we registered the smallest failure rate of sensors. The table below illustrates how the percentage of failure increase by changing some steps in the fabrication procedure:

Test	**Percentage of failure**	**Procedure**
1	24%	fast degassing
2	15%	peak pressure = -790mm Hg
3	10%	more than 3 cycles of degassing
4	1%/3%	following the procedure

Table 2.1: Percentage of sensor failure with the respect to the specific step of the procedure

We can conclude that fast degassing had the most relevant impact on sensor failure.The soft membrane inside the sensor chip can brake if subjected to abrupt change of pressure and cause the failure of the whole sensor.

2.4 Microprocessor and Control algorithm

An STM32f417 (144 pins, ARM Cortex-M4 with 1Mbyte Flash, 192kbytes of SRAM, 168 MHz, STmicroelectronics, Geneva, Switzerland) has been chosen to address all the signal and control the sensitive module.

The microprocessor was then connected to the sensitive module using 24 digital pin (GPIOD, GPIOA, GPIOE) plus V+ and ground.

The control algorithm is the sequent. The pressure values from the sensors is calibrated using algorithms provided by the sensor manufacturer, including gain and temperature correction .

$$P_{comp} = a_0 + (b_1 + c_{12}T_{adc})P_{adc} + b_2T_{adc} \tag{2.7}$$

The compensation algorithm is modified so that the final result was not rounded or scaled for atmospheric pressure.

For evaluating P_{comp} it is needed to start the sensor and then wait for a time that can vary from 1.8 to 3 ms to have the data available in the registers of the sensor. P_{comp} will produce a value of 0 with an input pressure of 50 kPa and will produce a full-scale value of 1023 with an input pressure of 115 kPa .

To inzialize UART and I2C the right PIN was clocked and a baud rate of 1 MHz and 400 kHz were chosen respectively. Then al the internal timer was inizialized. All the array was scanned to acquire the coefficient from each sensor.

The chip select was sequentially moved along the column and then along the row and while one sensor is selected the 4 coefficient were read and all the data stored in a matrix. A control test on the data read was made before to store the data. The chip select of the sensor was kept blocked high on one sensor until significant data is read.

Then the microcontroller before to start acquiring data from the sensors wait to be synchronized with the PC. Two specific character is waited in the UART register, once those characters arrived the acquisition loop can start.

The acquisition loop is divided in 5 parts that were cycled until an external break command is received:

- Collect data from the sensor and save them to temporary register using DMA access
- Convert all the data to the correspondent value in kPa
- Control if the data is significant
- Create the UART packet with the sensor data
- Send the packet

For collecting the data the microcontroller scan sequentially each row in the matrix sending before the start command to each sensor and then after a period of time that can vary from 1.5 to 3 ms scroll again the sensors to read the data. The data of each sensor is saved automatically without generating interrupt on the main execution of the program, so that the microcontroller is able to receive interrupt from other sources (ie interrupt from UART, or mechanical actuation), while the data is automatically updated in the correspondent registers. Then the data is converted to kPa and analyzed, if the data read is less than 60 kPa the data is read again.

The UART packet is the following Fig.2.22. It is composed by 86 byte:

The first and the last bytes are the control byte and will be controlled by the PC to ensure that the readings are correct. From the 2th to the

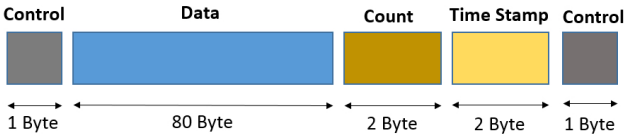

Figure 2.22: UART packet

81th bytes are sensor data, since each value of pressure is stored in a Float variable it is needed to have at least 4 byte to send one data, so with 20 sensors are needed at least 80 bytes of data. The last 4 bytes are the count value and the time stamp value, each one is stored in a 16 bit variable so it is needed 2 bytes for each one to send the information. Once the packet is composed it is sent sequentially over the UART Tx port.Then the loop restarted from the acquisition until a brake character is received in the UART Rx port.

Since the aim of the skin is to continuously acquire data from the prostate, the following table contain the performance of the acquisition algorithm on the specified STM32f4:

Time	1.5ms	3 ms
10 min	1%	0 %
30 min	5%	0,001%

Table 2.2: Percentage of data incorrect respect to the running time and the wait time between start and acquisition from the sensor

In table 2.2 the wait time between the start and the reading of the sensor was changed. With a wait time of 1.5ms that correspond to less than 6ms of the whole acquisition time, a failure of 0% and an error on the data read of 5% was registered on a 30 minute trial. With an increased wait time of 3ms that correspond to 12 ms of total acquisition time, the

error on the data goes down to almost 0,0000001% . The reason of this behavior can be found in that not all sensors are ready with a 1.5 ms of wait time.

Bendings	1.5ms	3 ms
10 min	1%	0 %
30 min	5%	0,001%

Table 2.3: Percentage of data incorrect respect to the running time and the wait time between start and acquisition from the sensor

2.5 Pc bridge and User Interface

To have data available on the PC a Bridge-Pc architecture was used Fig.2.23:

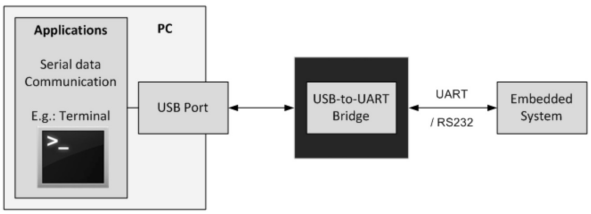

Figure 2.23: UART-USB bridge

We used as a UART-USB bridge.The main advantage of this architecture is the simplicity in using the FTDI libraries for getting data from the bridge. Since this is the first prototype it was chosen to pass trough the bridge instead of implementing a protocol using USB libraries for STM32.

The algoritm implemented for read the data from the bridge follow 4 step:

- Initialize variables and vectors
- Syncronize the PC with microcontroller

- Acquire and store data.
- Publish the data over Ethernet

In the first step all the variables were inizialized and the program wait until the user press a button to acquire the coefficient, once the button is pressed a communication acknologement is sent to the STM32 and the coefficients were stored.

Then the program wait the user to press again to synchronize device and Pc and once this condition is satisfied by pressing another button the acquisition loop starts.

The acquisition loop starts with a control on the first and the last value of the UART packet that was sent by STM32. If the packet is correct then all the data are converted to the correct value and displayed in the terminal window. The data are then written over an ethernet port a can be accessible from another computer connected over internet or local network.

The algorithm was tested on a Dell Optiflex 320. The mean loop time was recorded of 50 ms, The UART-USB was tested to value the error in the received packet with respect to the UART baud-rate. With a UART baud rate of 1 MHz no significant errors were found on the received packet so the architecture does not have a big impact on the performance of the system.

Subscriber/Publisher over TCP.

The TCP infrascructure is based on 0MQ framework. OMQ gives socket that carry messages across various transports, and in our case across TCP. The architecture that was implemented used OMQ libraries to connect socket N-to-N with a publisher-subscriber pattern.

The publisher/subscriber pattern is a one-way data distribution (figure 2.24).

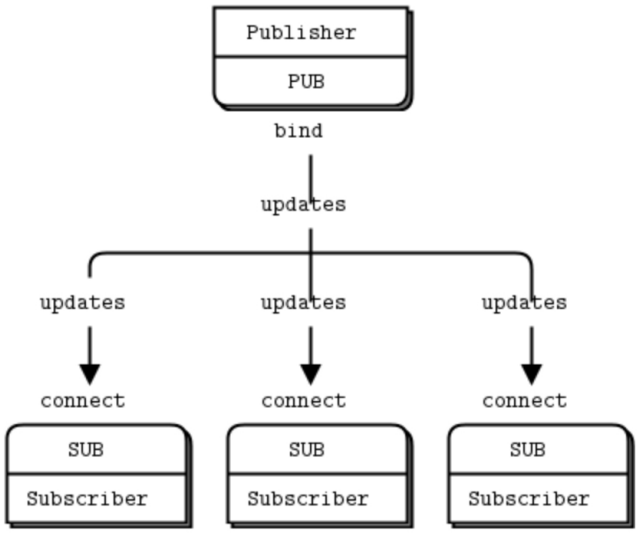

Figure 2.24: Publish-Subscribe

The publisher publishes the message over a pre-definite port and each subscriber can read the data that is written in that port. The big advantage of his architecture is that can be integrated perfectly in embedded system.

The reason why an TCP infrastructure was developed can be found in the needs of having multiple interface to control the device and to show the data that are collected during the experiment without the necessity of high computational performance.

User Interface

Since the bottom layer is composed by Subscriber/Publisher architecture, several user interfaces can be built to interface the data coming from the STM32.

One interface was built for visualizing the data in real time and to give an idea of which sensor was pressed Fig.2.25

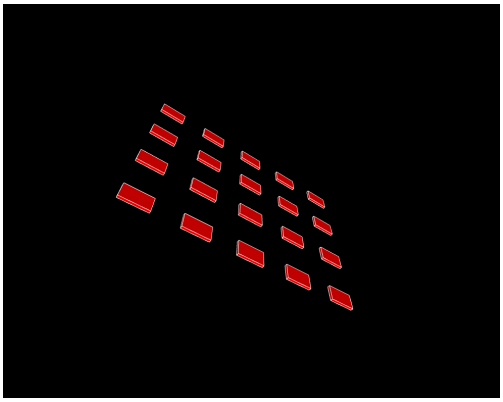

Figure 2.25: User interface

The array of values sent over ethernet, composed by the output pressure of each sensor, can be displayed using the graphical interface. Each segment symbolizes one sensor and changes its color depending on what is the i-th output pressure. The segment is red if no pressure is recorded and increase in yellow tonality proportionally to the input, so the maximum value will be decoded as a bright yellow.

Chapter 3

Calibration and Model validation

3.1 Model validation

The model is validated by comparing its result with the result obtained by experimental setup.

3.1.1 Results obtained by modelling

The mechanical model of the setup is shown in Fig 3.1, As aforementioned, the upper part of the Kelvin-Voigh model represents the thin layer of silicon on top of the PCB skeleton, the middle part represents the silicon between the tissue and the PCB and the third part represents the tissue that is palpated.

In order to validate the model two different set-ups were tested. The first trial is composed by the device against a rigid support, in this case we can omit the component of the model that represent the tissue as shown in Fig.3.2. The second trial is composed by device against a tissue

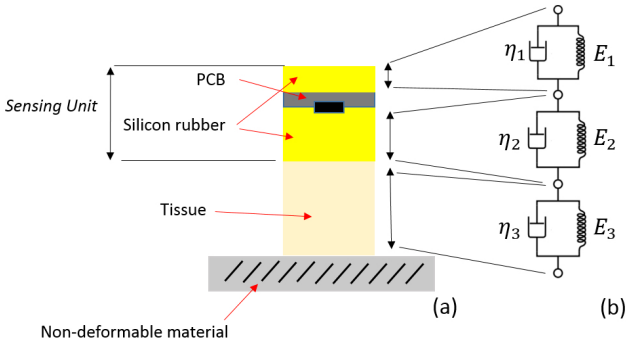

Figure 3.1: Model: a) the three parts of the sensing unit and the tissue b) the equivalent using Kelvin-Voight model

that has the same mechanical properties of the prostate without lump ($E = 21.2kPa$, $\eta = 750mPa * s$) and in this case all the components of the model were used.

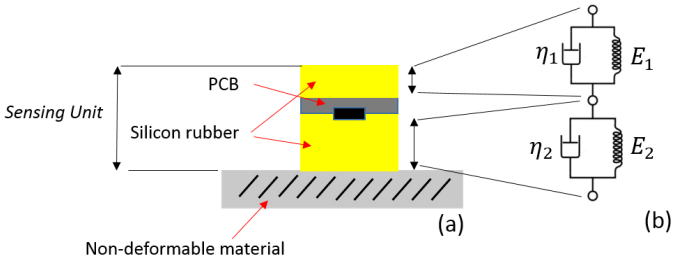

Figure 3.2: Model against rigid tissue: a) the three parts of the sensing unit, b) the equivalent using Kelvin-Voigh model

The transfer function V_{out}/V_{in} of the model is expressed by the following function:

$$H(s) = \frac{as^2 + bs + c}{ds^2 + es + f} \tag{3.1}$$

where taking in consideration that the elastic module and the viscosity of the silicon rubber is $E = 3,27MPa$ and $\eta = 23.000mPa*s$ respectively, we obtain $a = 2,35 * 10^{-12}, b = 2,71 * 10^{-05}, c = 0,088, d = 9,42 * 10^{-12}, e = 3,62 * 10^{-05}, f = 0,11$ for the trial with the tissue and $a =$

$0, b = 5.99 * 10^{-09}, c = 0.069, d = 0, e = 2.39 * 10^{-08}, f = 0.092$ for the experiment against rigid support.

The transfer function was obtained by finding the electric equivalent of the circuit as mentioned in chapter 3.1.

The transfer function evaluated in both cases for $s = 0$ gave this result: For the first trial $H(0) = 0.75$ and for the second $H(0) = 0.80$.

3.1.2 Results obtained by Experimental protocols

For the experiments a phantom of the same dimension and of the same elastic module of the tissue was made out of combining two ratios of liquid plastic and hardener (PVC Regular Liquid Plastic and Regular Liquid Plastic Hardener, MF Manufacturing, USA ,1-5 ratio). The sample was 30 mm thick with lateral sides of 100 mm.

For the first configurations the soft robotic skin was placed on a rigid support whereas for the second configuration the soft robotic skin was placed on the phantom.

Uniaxial palpation was performed on both configurations. A 3d printed rectangular probe was mounted on the end effector of the robotic manipulator and placed perpendicular to the phantom surface. The manipulator was programmed to perform indentations along the phantoms z-axes at a given sensor location. The robot started from a known point right above the sensor and moved down along the z-axis until it reached the soft robotic skin as indicated by the Force/Torque sensor installed on the end-effector. Then a fixed indentation was performed and the final value was kept stable for 24 sec to evaluate static gain of the system. Five trials were performed in both the configuration to evaluate the error.

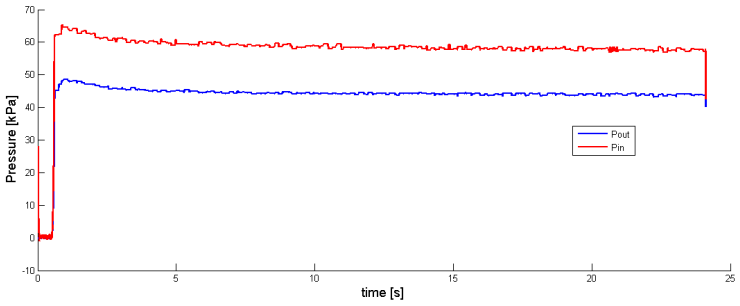

Figure 3.3: Model validation against rigid support

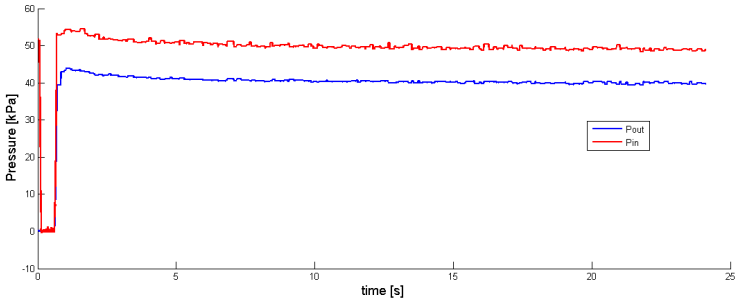

Figure 3.4: Model validation against tissue

The mean in five trials of both P_{in} calculated from the load cell, and P_{out} recorded from the sensor is represented in Fig.3.4 and 3.3.

The results in term of transfer function were $H(0) = 0.7591 \pm 0.037$ $H(0) = 0.8119 \pm 0.032$ respectively the first and the second trial.

3.1.3 Comparison of results

The experimental result were compared with the data from the model the maximum error respect to experimental data was $e = 0.043$ that correspond to the 4% as relative error. This error can be futerly reduced taking in consideration other parameters (i.e. Poisson corrective factor) that could help in finding a better estimation.

The data showed also that the sensitivity is higher in the second case

(i.e the trial against the tissue) with respect to the rigid support. This because the silicon is stiffer with respect to the tissue so the deformation is not equally distributed between skin and tissue. The part that is more rigid will deform less and will have less energy loss, so the skin is more sensitive against the tissue respect that against the rigid support.

3.2 Sensors Cross-talk, Sensitivity and spatial resolution

The reason why we have studied the cross talk between sensors is that there is a trade-off between number of sensors and flexibility of the device, The flexibility is inverse proportional to the number of sensors, in another words the flexibility decrease as the number of sensors increases. Hence it is needed to understand what is the number of sensors to avoid cross-talk between them.

Referring to [10] they studied the response of three MEMS sensor embedded in different silicone thickness. The sensors were soldered on a solid PCB at a fixed distance and in their study they focused their attention on understanding how the cross talk area increases with respect to the increasing in silicone thickness. The spatial impulse response from an array of sensors for different rubber thicknesses is presented in Fig.3.6. The results show that as rubber thickness increases, the strain distribution spreads laterally and the sensor loses sensitivity.

As aforementioned, the primary constrain for this project is to have a thickness of silicone that allows the surface to bend around the organ. For this purpose we studied the cross talk between two sensors taking in consideration only a fixed thickness of 3 mm for the sensing unit. The

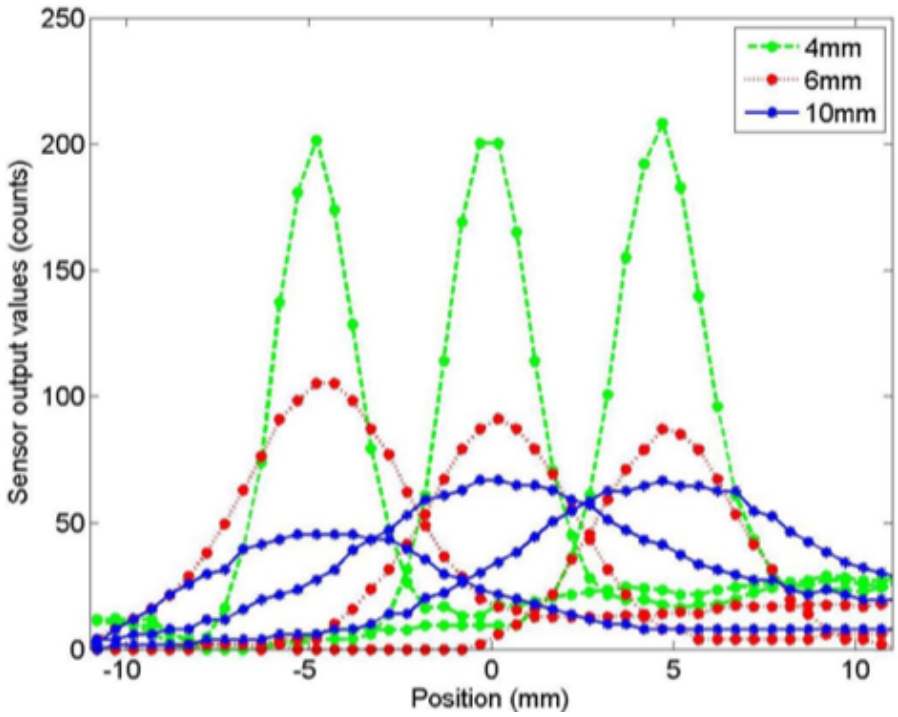

Figure 3.5: A spatial response to a scanned normal impulse for three sensors in each array with different rubber thicknesses

cross talk area sensors was then studied with respect to the distance between the sensors.

The spatial resolution was studied before and was found that it is around $3-5mm$ for a rubber thickness of 4mm [52].

3.2.1 Experiment

We choose to study the cross talk area with respect to 5mm, 8mm, 12mm between the sensing point of each sensors. For this purpose three PCB boards were made with the aforementioned distances.

A rolling probe was then attached to a robotic arm manipulator and a costant indentation was chosen. The arm was then moved with a costant velocity along the surface for 10 times and the data were then recorded and analyzed.

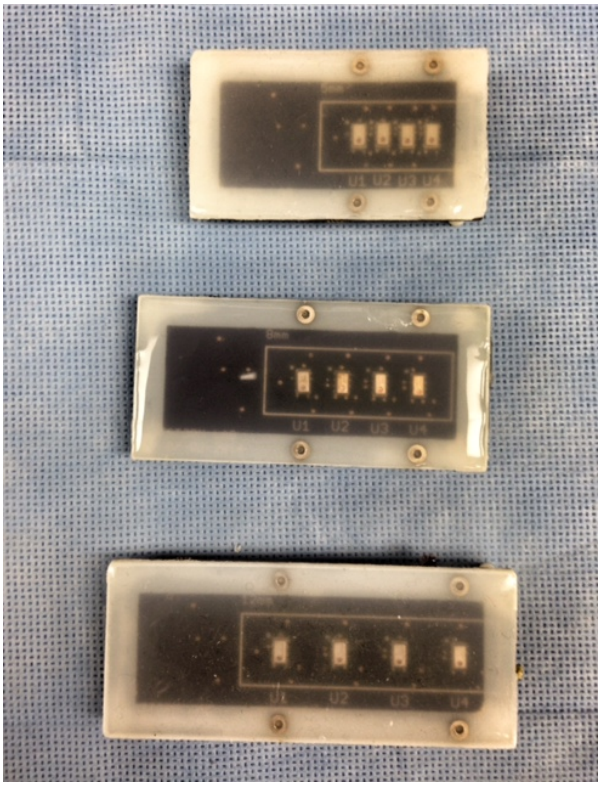

Figure 3.6: PCB board: with the same silicone thickness and different distance between sensors a) 5mm , b) 8mm, c)12mm

The spatial resolution was studied with respect to each sensor and was considered constant once the thickness of the silicon was chosen. The spatial response of the sensors was measured in terms of the impulse response. A constant force was applied sequentially along the line of sensors while the output was recorded for each sensor.

3.2.2 Results

The cross-talk was calculated choosing a threshold equal to 2 times the variance of the noise and then evaluating experimentally the area under the pressure curve of two sensors. Then the resulting area was expressed in percentage of the total area of the relative sensor.

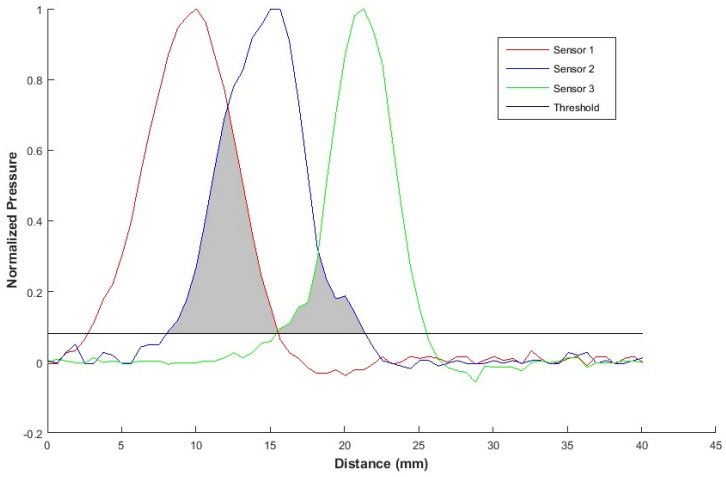

Figure 3.7: Cross talk area: 5mm distance between sensors

5 mm			
%CT 1_1	%CT 1_2	%CT 2_2	%CT 2_3
36.75	*37.93*	*14.85*	20.17

Table 3.1: 5mm: percentage of cross-talk with respect to the total area

The results were summarized in table 3.1, 3.2, 3.3, and the respective plots of 5mm, 8mm , 12mm are showed in figure 3.7, 3.8, 3.9.

The mean spatial resolution (i.e. the the distance from the sensing hole of the sensor in which the sensor can measure a variation of pressure) for the 5mm trial was $4.5mm \pm 0.2mm$. The sensitivity within the area goes from the highest value right above the pressure hole of the sensor to almost 0 on the border of the spatial resolution area.

8 mm			
%CT 1_1	%CT 1_2	%CT 2_2	%CT 2_3
4.01	*3.24*	*0.97*	0.74

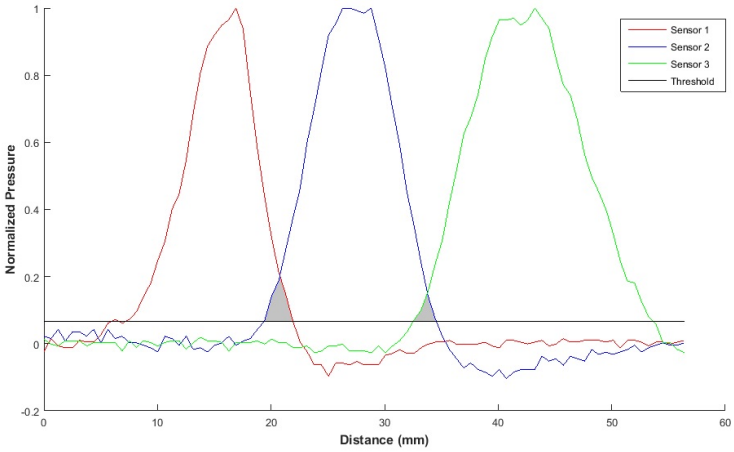

Figure 3.8: 8mm: percentage of cross-talk with respect to the total area

Table 3.2: 8mm: percentage of cross-talk with respect to the total area

The mean spatial resolution for the 8mm trial was $4.2mm \pm 0.5mm$.

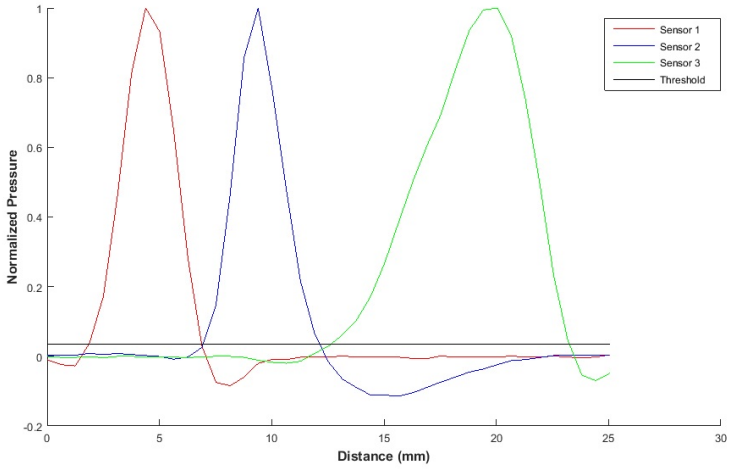

Figure 3.9: Cross talk area: 12mm distance between sensors

12 mm			
%CT 1_1	%CT 1_2	%CT 2_2	%CT 2_3
0	*0*	*0*	0

Table 3.3: 12mm: percentage of cross-talk with respect to the total area

The mean spatial resolution for the 12mm trial was $4.0mm \pm 0.4mm$

The results show that the average of cross talk-area decreases consistently as the distance between the sensors increase while the spatial resolution remain almost constant. The average cross talk readings in the 5, 8, and 10 mm trials was 27.42%, 2.24%, and 0%, respectively. This result shows that with a distance of 12mm there is not a measurable cross-talk between sensors, so that all the distances higher than 12mm are suitable for our purpose.

The sensitivity of one sensor after multiple trials results in $0.14 \pm 0.06kPa$ that corresponds to $0.011 \pm 0.0048N$ or $1.12 \pm 0.48g$.

3.3 Calibration

Under the hypothesis that the measurements are affected by the rubber nonlinearities, the sensor′ calibration requires the measurement of two quantities: $P_{out}(t)$, the sensor data, and $P_{in}(t)$, a known applied pressure used as a reference. As shown in Fig.3.10(a), if the soft robotic skin is pressed against a rigid non-deformable material, only the silicone rubber compresses due to $P_{in}(t)$.

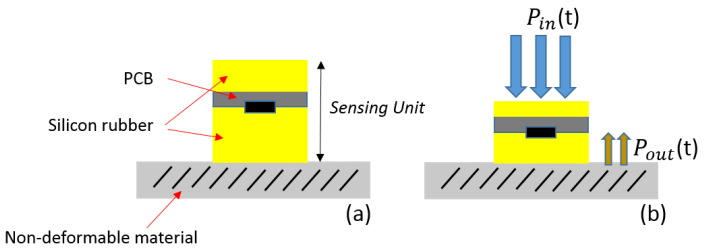

Figure 3.10: Schematic diagram of the calibration procedure at contact (a) and at an arbitrary instant of time (b) for a non-deformable material

As aforementioned, the pressure values from the sensors were calcu-

lated using algorithms provided by the sensor manufacturer, including gain and temperature correction. Then since the sensor are embedded in silicone the compensation algorithm was modified so that the final result was not rounded or scaled for atmospheric pressure. The external pressure was measured using a Torque Force sensor (NANO17, ATI Industrial Automation, Apex, NC, USA, resolution 1/160 N) installed on the end-effector of the robotic manipulator. Pressure readings were sampled at 125 Hz.

The calibration coefficient of each sensor was evaluated by dividing, in the instant of time in which the steady state is reached from every sensor, the average of pressure measured by the loadcell by the average of pressure measured by the sensors.

3.3.1 Test bench

A 3d printed rectangular probe ($A = 81mm^2$) was mounted on the end effector of the robotic manipulator and placed perpendicular to the phantom surface. The manipulator was programmed to perform indentations along the z-axes throughout the entire sensor array at known sensor locations. The robot started from a known point right above the first sensor and moved down along the z-axis until it reached the soft robotic skin as indicated by the Force/Torque sensor installed on the end-effector. Then a fixed indentation was performed and the final value was kept stable until the response of the system reached the steady state. Then the robot moved back to the original position and another sensor of the array was tested with the same protocol. The whole protocol was repeated five times.

3.3.2 Results

With a fixed indentation of 0.30 mm the results are shown in Fig.3.11:

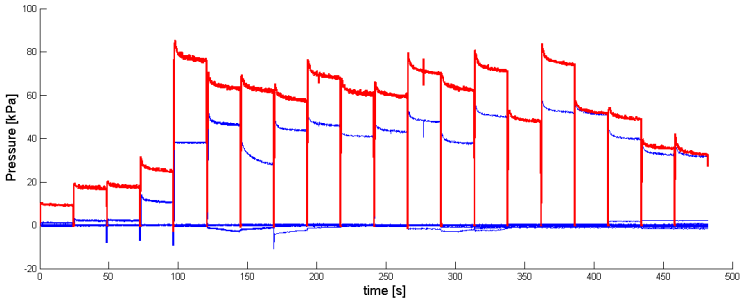

Figure 3.11: Force/torque value (red) and i-th sensor (blue) in every instant of palpation before calibration

Due to fabrication imperfections even if the indentation is the same in all the experiment, the measured pressure from the external Force/Torque sensor is not the same for all the sensors, in other word every sensors needs to be calibrated separately.

The sensors of the first row, that are the first 4 starting from left in the graph, will not be considered for the sequent analysis since their reference pressure cannot be compared with the other. This result can be associated to the fact that the first row is next to the connectors so that it is not in perfect contact with the rigid support, and that causes a completely different reading from the F/T sensor.

The other sensors were analysed and calibrated after the steady state response was reached. For the sensors that the calibration were not possible on the previous trial (i.e. sensors 5,7,15) due to the not correct palpation point, or to digital saturation, another trial was made and the coefficient was calculated on that trial.

The mean calibration coefficient was 0.742 ± 0.08. After that the coefficients were applied, all the sensors were successfully calibrated. Fig.

3.12

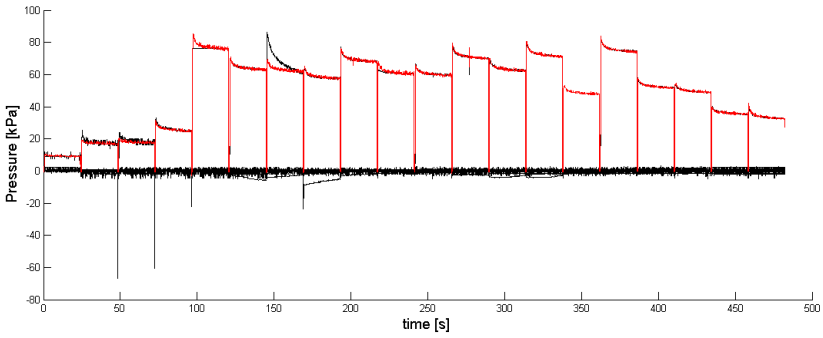

Figure 3.12: Force/torque value (red) and i-th sensor (blue) in every instant of palpation after calibration.

After the calibration the error of pressure out with respect to the reference was less than $0,01kPa$ for all the sensors.

Chapter 4

Soft Robotic Skin: Test and Results

4.1 Performance assessment

The sensitivity and the resolution of the resulting sensitive sub-module was evaluated by applying a load to the rubber directly behind the sensor using a probe with a squared tip with an area of $81mm^2$. The load was applied incrementally until the sensor output was saturated. Then the load was gradually removed to evaluate the hysteresis of the sensor. The typical interval between load changes was 1 sec, and the total interval for loading and unloading of each sensor was approximately 5 min. The process was repeated for each sensor in matrix

4.1.1 Results

All sensing head showed a different full scale range that can be summarized on the following table:

Flexible skin			
Sensor 1	***Sensor 2***	***Sensor 3***	***Sensor 4***
131 kPa	*140 kPa*	*151 kPa*	*143kPa*
0.12 kPa	*0.13 kPa*	*0.15 kPa*	*0.13 kPa*
Sensor 5	***Sensor 6***	***Sensor 7***	***Sensor 8***
146 kPa	*154 kPa*	*146 kPa*	*148 kPa*
0.14 kPa	*0.15 kPa*	*0.14 kPa*	*0.14 kPa*
Sensor 9	***Sensor 10***	***Sensor 11***	***Sensor 12***
147 kPa	*150 kPa*	*148 kPa*	*146 kPa*
0.14 kPa	*0.14 kPa*	*0.14 kPa*	*0.14 kPa*
Sensor 13	***Sensor 14***	***Sensor 15***	***Sensor 16***
148 kPa	*146 kPa*	*145 kPa*	*150 kPa*
0.14 kPa	*0.14 kPa*	*0.14 kPa*	*0.15 kPa*
Sensor 17	***Sensor 18***	***Sensor 19***	***Sensor 20***
149 kPa	*148 kPa*	*146 kPa*	*145 kPa*
0.14 kPa	*0.14 kPa*	*0.14 kPa*	*0.14 kPa*

Table 4.1: Full scale range and Resolution of each row of the array.

The useful pressure measurement range appears to be larger than stated in the data sheet and varies from a pressure of 138.2 kPa to a pressure of 151.2 kPa, well above the maximum of data sheet 115 kPa. The effects of regularly exceeding the specified maximum are not clear; Other studies were made and the results have shown no degradation in performance under thousands of loading cycles and under repeated loads above ten times saturation [52].

Each sensor output showed a fast response and no hysteresis. The experiments have shown that the full step response invariably occurs within two samples or 10 ms and also the sensor output variation is highly linear

($r^2 > 0.99$ for all the sensors) with ambient temperature 20-26 C. The manufacturer provides a temperature compensation algorithm using the onboard temperature sensor for use in the air, but it is not accurate for sensors cast in rubber. As [52] The linearity suggests that a simple linear compensation scheme is adequate, although high accuracy may require the determination of the specific calibration coefficient for each sensor.

The standard deviation of the noise was recorded from all the 20 unloaded sensors at 120 Hz for 60 s.

Flexible skin			
Sensor 1	***Sensor 2***	***Sensor 3***	***Sensor 4***
0.03 kPa	*0.05 kPa*	*0.04 kPa*	*0.05 kPa*
Sensor 5	***Sensor 6***	***Sensor 7***	***Sensor 8***
0.05 kPa	*0.04 kPa*	*0.04 kPa*	*0.05 kPa*
Sensor 9	***Sensor 10***	***Sensor 11***	***Sensor 12***
0.05 kPa	*0.05 kPa*	*0.05 kPa*	*0.04 kPa*
Sensor 13	***Sensor 14***	***Sensor 15***	***Sensor 16***
0.04 kPa	*0.02 kPa*	*0.05 kPa*	*0.09 kPa*
Sensor 17	***Sensor 18***	***Sensor 19***	***Sensor 20***
0.05 kPa	*0.03 kPa*	*0.04 kPa*	*0.05 kPa*

Table 4.2: Standard deviation of noise on each sensor.

The overall average root-mean-square noise was $0.1125kPa$ with a standard deviation of $0.08kPa$. This corresponds to an applied load of $0.001N$ or $0,01g$. These noise levels are small with respect to the measurement range of the sensor, and simple filtering can further reduce the effects of the noise if a more accuracy is needed.

4.2 Test bench

4.2.1 Phantom preparation

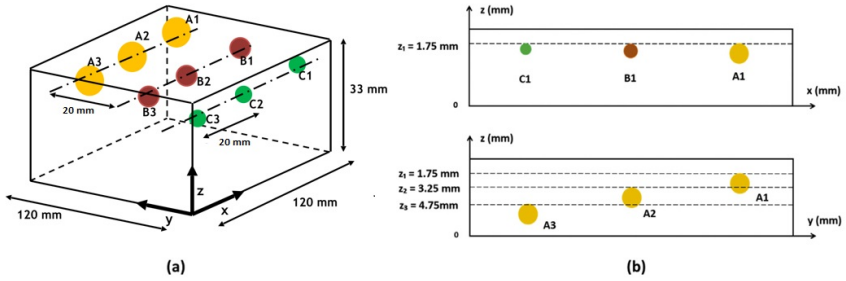

Figure 4.1: Dimensions of the fabricated phantoms with the embedded lump locations (a) and their relative depth (b)

The SRS ability to detect different stiffness was tested on one synthetic sample. The sample was fabricated by combining two ratios of liquid plastic and hardener (PVC Regular Liquid Plastic and Regular Liquid Plastic Hardener, MF Manufacturing, USA ,1-5 ratio). The sample is 30 mm thick with lateral sides of 100 mm. As in the previous trials, the soft robotic skin was placed on the tissue sample and a rectangular probe was mounted on the distal side of the load cell to indent the samples. Five loading/unloading trials reaching a fixed indentation dept approx the 10% of the sample thickness were performed to the tissue sample at a constant speed of 1 mm/s. When the maximum value of indentation was reached it was kept fixed for 30 sec to evaluate the system when the steady state was reached.

The stiffnesses measured by the load cell were equal to $E = 21.2kPa$. Experimental plots obtained from a single loading are represented in Fig.4.2. The results show that the Soft robotic skin was effective in de-

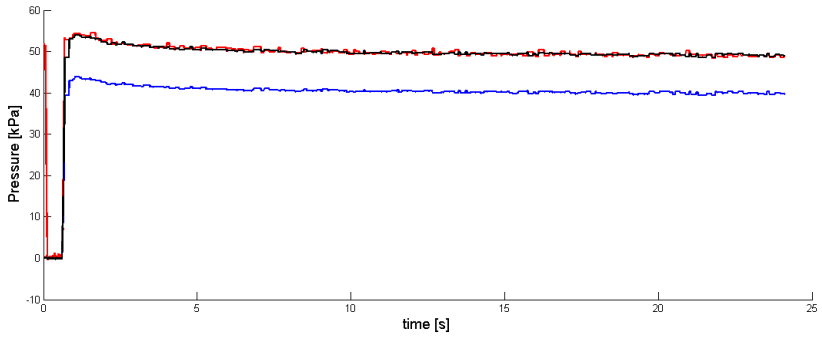

Figure 4.2: In red the stiffness measured by the Load cell, in blue the pressures obtained by the sensor, in black the stiffness estimated by the model

tecting the stiffness of the tissue sample with an average relative error equal to $4.4 \pm 0.1\%$.

4.3 Robotic Test

4.3.1 Experimental Protocol

The elastic moduli of the on silicone phantom was measured by conducting multiple indentation tests on the tumor-free areas, and resulted as $PH = 21.78 \pm 1.45kPa$. This value is typical for prostate′s tissue, as reported [14]. Uniaxial palpation was performed on the phantom with the rectangular probe mounted on the end effector of the robotic manipulator and perpendicular to the phantom′s surface. Two different trials were made:

- For the first trial, the manipulator was programmed to perform indentations along the phantoms′ x-axes and y-axes at intervals equivalent to the distance between two sensors (i.e 2cm), in other word the manipulator was programmed to apply a load behind each sensors.

- For the second trials, the intervals were 6 mm (1/4 of the distance between sensors) to increase the spatial resolution.

For both the trials an $r \times c$ matrix of indentation points was created. The number of points for each row was set equal to the number of columns, creating an area of about $60 \times 60mm$ of indentation. The first experiment had $r_{d1} = c_{d1} = 4$ row and column combinations, resulting in 4×4 indentation points whereas the second experiment had $r_{d2} = c_{d2} = 10$, and that creates a matrix of 10×10. Placing the origin at the phantom′s corner, the first indentation point P0, was set at x = 12 cm and y = 12 cm that correspond to 5^{th} sensor on the SRS (that is the origin of the Cartesian system of the SRS). Fig 4.3.

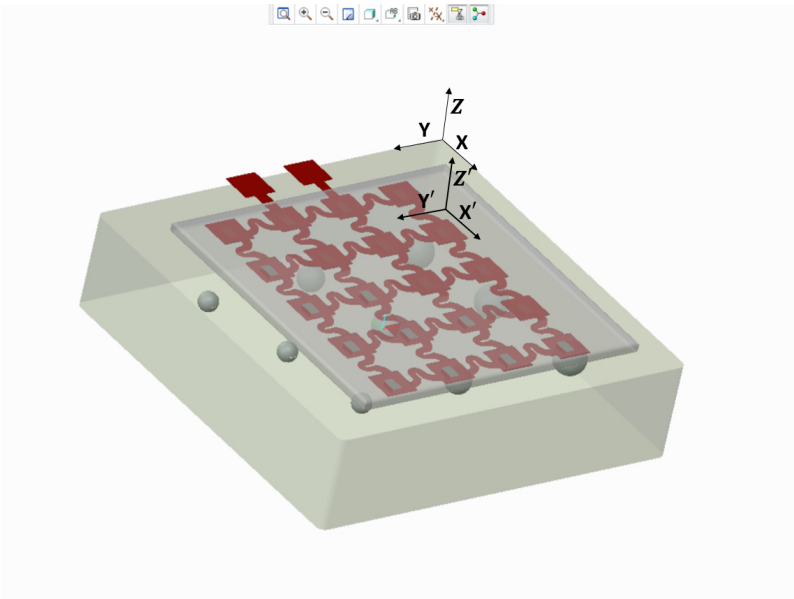

Figure 4.3: SRS placed on the tissue phantom: The cartesian system of the phantom and of the SRS

The SRS surface is not perfectly even, thus the contact point with the surface needs to be estimated for each of the indented points. Therefore, before the start of the palpation procedure, the standard deviation of the

F/T sensor measurements was calculated with no load applied. The probe then approached the SRS surface from a distance of about 20 mm and a speed of 2 mm/s until the Force measurement exceeded three times its standard deviation. When this condition was verified, the manipulator z position was assumed to be in contact with the phantom surface. Then, the Probe indented the SRS and the phantom at a speed of 1 mm/s until the programmed indentation depth was achieved.

Motion in the opposite direction with the same speed was performed until the probe returned to the depth of the contact point. Here, the probe was moved 20 mm up from the surface and then shifted along the phantom′s x-axis to the next indentation point. This procedure was repeated c times (equal to the number of columns in the indentation matrix) before the manipulator shifted along the phantom′s y-axis to begin a new path. The SRS were found to have an uneven surface with average surface height along their z-axes of $4 \pm 0.64mm$ and $4 \pm 0.54mm$, respectively.

To evaluate the robustness and repeatability of the SRS, both indentation palpation trials were repeated five times with an indentation depth of 3 mm.

4.3.2 Results

After completion of the palpation experiments, pressure maps of the phantom for 3 mm of indentation depth in both trials were generated. Embedded lumps are stiffer than the surrounding silicone, and their location in the map is represented by a higher stiffness region (red). The results from the first trial (i.e 4x4 matrix, 16 indentation points spaced by 20 mm) is shown in Fig.4.4.

The sensor′s pressure map is the matrix that contains all the stiffness

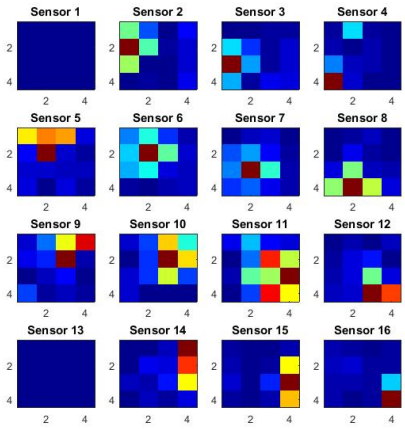

Figure 4.4: Sensors pressure maps: made by 16 indentation points each one behind a specific sensor

values recorded by a specific sensor in all the indentation points of the experiment after that the predicted value from the model was subtracted. This result is still corrupted by noise since the accuracy of the sensors is in air, as mentioned on the data sheet, equal to $\pm 1kPa$ so each pressures map has been filtered with a specific threshold that is the sum of the minimum pressure measured by each maps and 5 times the sensor standard deviation. The result is shown in Fig.4.5

We can summarize the results of this trial:

- Since the pressure was applied right behind each sensor and as mentioned in chapter 2.1 this is the point where each sensor sensitivity is highest, the average resulting lump detection success rate was equal to 100%.

- The location of each sensor is fixed in the space, and so the spatial resolution is fixed to 20 mm, and with this spatial resolution we were not able to characterize the effectiveness of the device in detecting the exact position of the lumps.

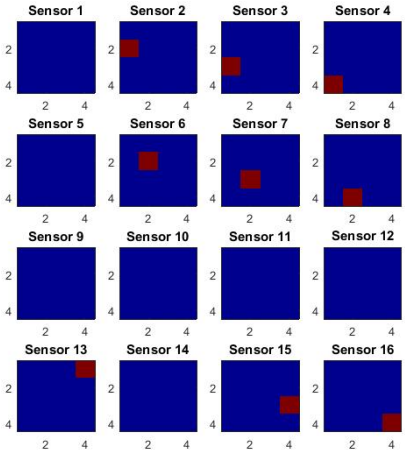

Figure 4.5: Sensors pressure maps after the threshold was applied: made by 16 indentation points each one behind a specific sensor

Fig.4.6 shows the map obtained from the second trial (i.e 10x10 matrix, 100 indentation points spaced by 6mm).

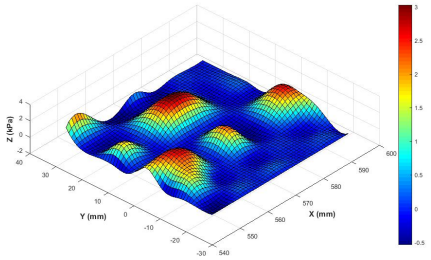

Figure 4.6: Stiffness map obtained after interpolating the data

The final map was obtained by interpolating the result obtained by summing all the filtered pressures of each sensor.

Fig.4.7 shows the pressures map of each sensor before removing the noise. The filtered results are showed in fig 4.8.

The plot in Fig.4.6 consisted only of the regions where the indentation pressure exceeded a certain threshold, in this case, the sum of the minimum pressure measured by the map and 5 times the sensor standard

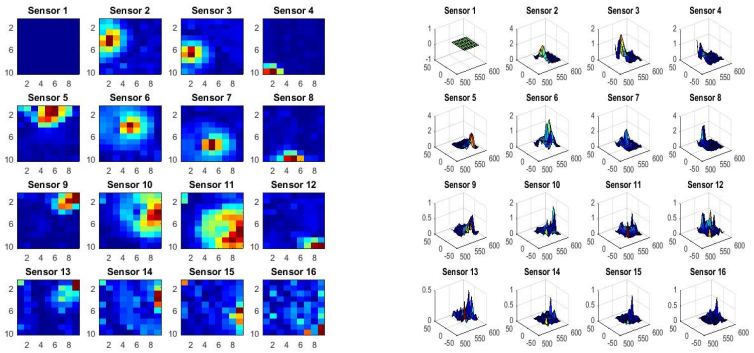

Figure 4.7: Unfiltered pressures maps

deviation.

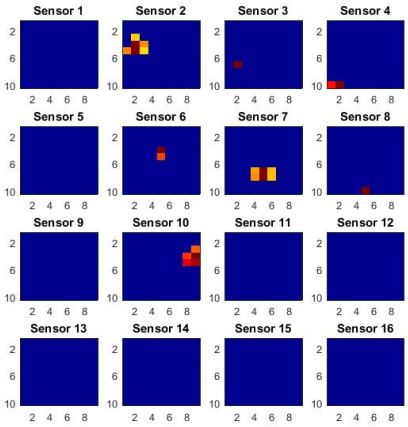

Figure 4.8: Filtered pressure maps.

In the second trial seven out of nine lumps were identified. In this case there is no correlation between indentations points and location of the sensors as it was before, meaning that the indentation points are with different sensitivity, so that not all the lumps were identified.

The effectiveness of the SRS in detecting different size lumps is reported by the average errors between the stiffness peaks and the lumps center locations along with the average detected lump area for all the

trials. Overall, for the second trial, the average relative location error in detecting the lumps was equal to $E_x = 3.2mm$, $E_y = 1.2mm$ that correspond to 0.16% and 0.06% of relative error.. The resulting average resulting lump detection success rate was equal to 77%. The results suggest that the number of visible embedded lumps in the map increases with indentation depth and so with higher pressure applied.

We were not able to identify the dept and the area of the lumps, since them depends on the sensitivity that is non constant in the whole surface, and to make it constant it is needed to know the area of actuation and the maximum input pressure (that correspond to an indentation) that the actuation unit can provide.

4.4 MIS simulator Test

In the last trial the phantom and the SRS were placed inside a MIS training box, as shown in Fig.4.9

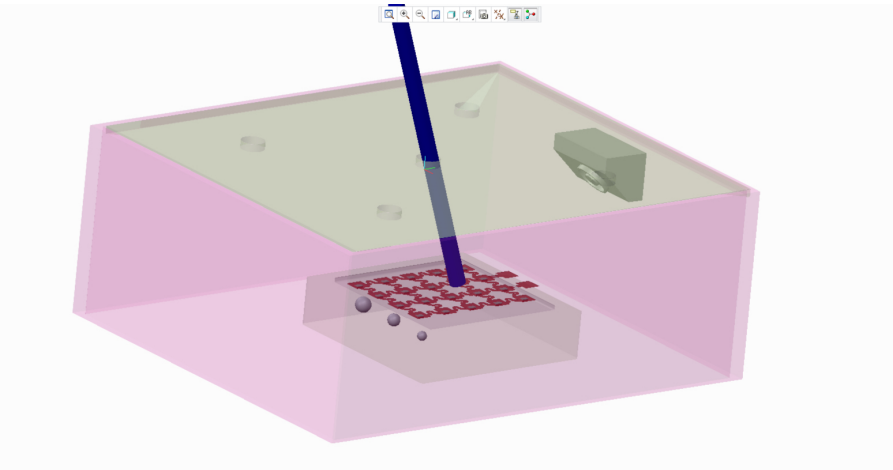

Figure 4.9: MIS simulator box for the experiment.

With respect to the robotic test in this case a different phantom was used. The phantom has a dimension of $120mm \times 120mm$ and a thickness

of 12.7mm. The tumor-free areas have the same elastic modulus $E = 21kPa$ of the prostate. It has 3 embedded lumps placed at the same dept $2mm$, with a distance of $2cm$ and with different sizes. The lumps have a diameter of $10mm$, $8mm$, $6mm$ respectively.

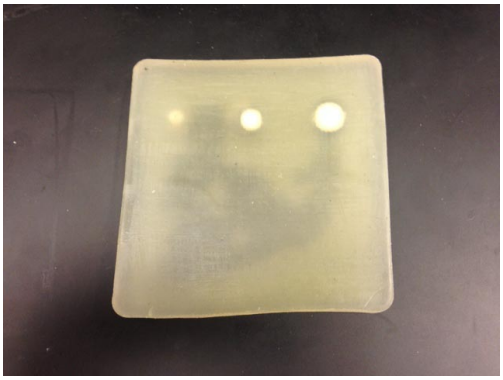

Figure 4.10: MIS simulator box trial: phantom with 10mm, 8mm, 6mm lumps embedded

4.4.1 Experimental protocol

With a laparoscopic grasper the surgeon performed indentations along the phantoms′ x-axes and y-axes at intervals equivalent to the distance between two sensors (i.e 2cm). Even if the indentation was not measured, we tried to keep the load applied constant in all the indentation points counting 2 s after the touch was reached and assuming the speed of indentation almost constant for all the experiment. During all the experiment the values of pressures of each point were showed in the user interface with a colour scale as explained in chapter 2.25.

4.4.2 Results

The maximum value of pressure recorded was taken from each sensor and compared with the predicted value obtained by the model. The input value of the model (P_{in}) was estimated as the pressure that correspond to

the indentation reached after 2 s taking in consideration a constant speed during the movement. All the points were than interpolated to create a continuous map of pressures.

The results are showed in Fig.4.11

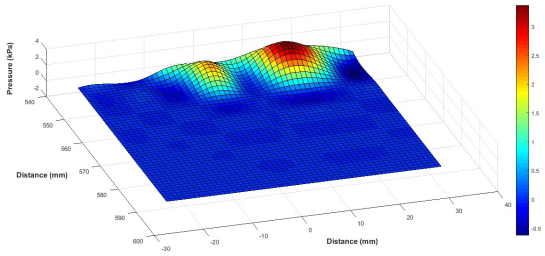

Figure 4.11: MIS simulator box trial: two lumps were identified that correspond to a resulting lump detection success rate equal to 66%

Two out of three lumps were identified with success that correspond to a resulting lump detection success rate equal to 66%, as in the previous trial the SRS showed problems in identify lumps with diameter equal to 6 mm independently of the deep, but showed no problem with both the 8mm and the 10 mm.

Since the SRS was placed without any reference respect to the phantom all the distance were calculated respect to 4^{th} sensor that is the origin of reference system of the SRS.

The area detected for the $10mm$ and the $8mm$ lump was $201mm^2$ and $153.2mm^2$ that means a relative error in identifying the area of 35% and 23% respectively. The distance on the x-axis between the peak of the two lumps is 20mm with an error of $E_x = 0.5mm$ and $E_y = 0.5mm$ that corresponds to the 0.025% of relative error.

Chapter 5

Conclusion and Future Development

5.1 Summary of Thesis Achievements

A flexible sensing module for the Soft Robotic Skin had been designed, fabricated, characterized and tested in order to localize tumors inside the prostate.

For what concerning the design and the fabrication, the module results $104mm \times 70mm$ and 4mm in thickness. It is composed by taxels of $9 \times 9mm$ connected by meandering wires that allow a higher elongation of the part before failure if compared to straight wires. The communication has always been stable and reliable since the interface of the sensors is a digital signal over a standard bus, this characteristic allowed us to interconnect more sensors on the same bus without having noise problems or analog stages to acquire the data. All this features together let us to save signal lines and allow us to decrease the dimensions of the devices.

The device was characterized in term of performance. The final results can be summarized in:

- The MEMS barometer chips can be used as contact pressure sensors. The conversion requires only vacuum degassing during rubber overmolding. All the resulting transducers are highly sensitive, with response as low as about one gram-force (0.01 N). They showed a fast response and no hysteresis, the avarage standard deviation of the noise was about 0.01 gram-force (0.001N). These noise levels are small with respect to the measurement range of the sensor, and simple filtering can further reduce the effects of the noise if a more accuracy is needed.

- The average mean spatial resolution areas that is centered on the ventilation hole of each sensors is $56mm^2$ that correspond to a radius of 4.2 mm when the module is placed on a rigid support and is $1256mm^2$ on the prostate tissue that correspond to a radius of 2 cm. This behaviour is explained by the elastic module of the prostate tissue that allow the module to bend more with respect to the rigid support.

- The sensitivity varies along the spatial resolution area and depends on the rubber thickness and on both the material and the tissue elastic module. With the thickness of 3 mm the sensitivity has the peak right above the ventilation hole of each sensors and decrease exponentially until reach a zero value on the edge of the spatial resolution area, this means that depending on what part is pressed the sensitivity changes. This implies an issue if the values of stiffness measured have to be compared between them. The sensitivity varies also with respect to the materials, as shown in that chapter **??**.The transfer function against rigid support and tissue are 0.75 and 0.81 respectively. This result show that if the palpated material is softer than the silicon rubber there is less energy loss during the process

that imply an higher dynamic to detect variation in stiffness.

- All the sensors needs to be calibrated singularly because as shown in chapter 3 every sensor has a different dynamics that depend on the fabrication procedures (thickness of the material, degassing procedures). After the calibration procedure the overall mean error with respect the reference sensor is $0,01kPa$ for all the sensors.

- The Kelvin-Voight model can be used to describe the behaviour of the system with an accuracy of 5%. In all the thesis it was used to predict the steady state response of the system and needs additional corrective factor that are material-dependent to estimate with more accuracy the dynamics and the static of the system.

The Final tests showed that

- The Soft robotic skin was effective in detecting the stiffness of the tissue sample with an average relative error equal to 4.4%.

- The overall lump detection success rate in all the experiment presented is equal to 81% with an overall error of identification of $E_x = 1.85mm$, $E_y = 0.85mm$ that correspond to 0.09% and 0.04% of relative error. The Lumps with 10 mm and 8 mm of diameter were always identified independently of the dept with a overall relative error in estimate the area of 35% and 23% respectively, the 6 mm lumps were identified with an overall rate of 0.25% but the data were not reliable enough to calculate the area.

The prototype of the sensitive module has proved to be effective in detecting the change in stiffness with an error and a detection rate that is comparable with the other methods illustrated in Cap.1.4. With respect to the TRUS that are widely used for detecting nodules in the organ, the

mechanical map obtained by palpation is proven to be more reliable and suffer less the location errors caused by the dimension and the location of the prostate. So this method is in general more accurate in detecting the presence of lumps and can give important information about their location. In addition, the mechanical map is obtained by autonomous palpation without the assistance of a surgeon and this resolves the issues related to the manoeuvrability of the device during the operation.

5.2 Conclusion and Future work

In conlusion the development of the sensing module is the starting point to prove the feasibility of a intraoperative soft robotic palpation of the prostate. The results showed that it is possible to detect lumps inside the tissue using this method but some improvements are needed obtain more reliability on the data.

An optimized second version of this module can be developed taking in consideration the following:

- The area of displacement of the actuation unit, which is necessary to improve the sensibility of the device.
- The range of pressures (and the consequent range of displacements) that can be provided from the actuation unit.
- Different silicone rubbers that are stiffer with respect to the current one to improve the transfer function and have less loss of energy.
- A lower thicnkess of the silicone layers, to improve the flexibility of the device.

Future studies will be made to fabricate and characterize the Actuation and the Anchoring module. In particular studies on soft robotic

actuation will aim at designing the air chamber and in general to control the displacement of the Sensing module.

Bibliography

[1] S. Standring, 2008, Grays Anatomy: The Anatomical Basis of Clinical Practice, 40 ed., Churchill Livingstone, London, England.

[2] http://www.medixselect.com/page/averageprostatesize

[3] J. Walz, A.L¿ Burnett, A.J. Costello, J.A. Eastham, M.Graefen, B. Guillonneau, M. Menon, F. Montorsi, R.P. Myers, B. Rocco, A. Villers. A Critical Analysis of the Current Knowledge of Surgical Anatomy Related to Optimization of Cancer Control and Preservation of Continence and Erection in Candidates for Radical Prostatectomy. European Urology 2010; (57);179-192.

[4] D.R. Kaye, M.E. Hyndman, R.L. Segal, L.Z. Metter, B.J. Trock, Z. Feng, L.M. Su, T.J. Bivalacqua, C.P. Pavlovich. Urinary outcomes are significantly affected by nerve sparing quality during radical prostatectomy, Urology, 2013 Dec;82(6):1348-53.

[5] Costello AJ, Brooks M, Cole OJ. Anatomical studies of the neurovascular bundle and cavernosal nerves. BJU Int 2004;94:10716.

[6] A. Jemal, F. Bray, M. Center, J. Ferlay, E. Ward, D. Forman. Global Cancer Statistics, CA Cancer J Clin 2011;61:6990.

[7] Surveillance Epidemiology and End Results (SEER), National Cancer Institute website, http://seer.cancer.gov/statfacts/html/livibd.html

[8] L. Bubendorf, A. Schpfer, U. Wagner, G. Sauter, H. Moch, N. Willi, T.C. Gasser, M.J. Mihatsch. Metastatic patterns of prostate cancer: an autopsy study of 1,589 patients, Hum Pathol. 2000 May;31(5):578-83.

[9] National Cancer Institute website, http://www.cancer.org/cancer/prostatecancer/detailedguide/prostate-cancer-treating-surgery

[10] J. Finkelstein, E. Eckersberger, H. Sadri, S. Taneja, H. Lepor, B. Djavan. Open Versus Laparoscopic Versus Robot-Assisted Laparoscopic Prostatectomy: The European and US Experience. Reviews in Urology. 2010;12(1):35-43.

[11] J. Fuller, W. Scott, B. Ashar, J. Corrado, Laparoscopic trocar injuries: A report from a U.S. Food and Drug Administration (FDA) Center for Devices and Radiological Health (CDRH) Systematic Technology Assessment of Medical Products (STAMP) committee, 2003; U.S. Food and Drug Administration website,

[12] National Cancer Institute, 2012. Prostate-Specific Antigen (PSA) Test, from http://www.cancer.gov/cancertopics/factsheet/detection/PSA

[13] D.C. Dugdale, 2011. Digital Rectal Exam, from http://www.nlm.nih.gov/medlineplus/ency/article/007069.htm

[14] Leigh A. Baumgart, Gregory J. Gerling*, and Ellen J. Bass. Characterizing the range of simulated prostate abnormalities palpable by digital rectal examination.Cancer Epidemiol. 2010 February

[15] National Institutes of Health, 2013. Panel endorses active monitoring and delay of treatment for low-risk prostate cancer, from http://www.nlm.nih.gov/medlineplus/ency/article/007069.htm

[16] National Cancer Institute. Gleason Score, from http://www.cancer.gov/dictionarycdrid=45696

[17] M. Roach, III, V. Weinberg, M. Nash, H.M. Sandler, P.W. McLaughlin, M.W. Kattan. Defining High Risk Prostate Cancer With Risk Groups and Nomograms: Implication for Designing Clinical Trials. Journal of Urology, 2006; (176);S16-S20.

[18] J. Finkelstein, E. Eckersberger, H. Sadri, S. Taneja, H. Lepor, B. Djavan. Open Versus Laparoscopic Versus Robot-Assisted Laparoscopic Prostatectomy: The European and US Experience. Reviews in Urology. 2010;12(1):35-43.

[19] J. Fuller, W. Scott, B. Ashar, J. Corrado, Laparoscopic trocar injuries: A report from a U.S. Food and Drug Administration (FDA) Center for Devices and Radiological Health (CDRH) Systematic Technology Assessment of Medical Products (STAMP) committee, 2003; U.S. Food and Drug Administration website, http://www.fda.gov/medicaldevices/safety/alertsandnotices/ucm197339.htm

[20] R.F. Coelho, B. Rocco, M.B. Patel, M.A. Orvieto, S. Chauhan, V. Ficarra, S. Melegari, K.J. Palmer, V.R. Patel. Retropubic, laparoscopic, and robot-assisted radical prostatectomy: a critical re-

view of outcomes reported by high-volume centers, J Endourol. 2010 Dec;24(12):2003-15.

[21] Intuitive Surgical, Inc., http://www.intuitivesurgical.com

[22] A. Papachristos, M. Basto, L. Te Marvelde, D. Moon. Laparoscopic versus robot-assisted radical prostatectomy: an Austalian single-surgeon series, ANZ J Surg. 2014 Apr 15.

[23] Canes, David, et al. "The future of NOTES instrumentation: flexible robotics and in vivo minirobots." Journal of endourology 23.5 (2009): 787-792.

[24] http://www.davincisurgery.com/da-vinci-urology/da-vinci-procedures/da-vinci-prostatectomy/

[25] J.H. Witt, V. Zugor, C. Wagner, A. Schutte, A.P. Labanaris. Robot-Assisted Radical Prostatectomy, Laparoscopy An Interdisciplinary Approach, Dr. Ivo Meinhold-Heerlein (Ed.), ISBN: 978-953-307-299-9, InTech, Available from: http://www.intechopen.com/books/laparoscopy-an-interdisciplinary-approach/robot-assisted-radical-prostatectomy

[26] Department of Urology Tuebingen, 2009. da Vinci Prostatectomy, from http://davinci-suedwest.de/da-vinci-surgery-the-prostatectomy.html

[27] Mayo Clinic Health System, 2013. Robotic Services, from http://mayoclinichealthsystem.org/locations/eau-claire/medical-services/surgery/robotic-surgery/robotic-services

[28] Department of Urology, University of Patras. Extraperitoneal Robotic-assisted Radical Prostatectomy, from

http://www.laparoscopy-endourology.com/main/clinical-expertise/robotic-surgery/extraperitoneal-robotic/

[29] D.R. Kaye, M.E. Hyndman, R.L. Segal, L.Z. Metter, B.J. Trock, Z. Feng, L.M. Su, T.J. Bivalacqua, C.P. Pavlovich. Urinary outcomes are significantly affected by nerve sparing quality during radical prostatectomy, Urology, 2013 Dec;82(6):1348-53.

[30] A. Gupta, M. Han. Imaging guidance in minimally invasive prostatectomy, Urol Oncol, 29(2011) 343-346.

[31] P. Dario and M. Bergamasco, An advanced robot system for automated diagnostic tasks through palpation, IEEE Trans. Biomed. Eng., vol. 35, no. 2, pp. 118126, Feb. 1988.

[32] R.Howe,W.Peine,D.Kantarinis,andJ.Son,Remotepalpationtechnology, IEEE Eng. Med. Biol. Mag., vol. 14, no. 3, pp. 318323, May/Jun. 1995.

[33] T. Ohtsuka, A. Furuse, T. Kohno, J. Nakajima, K. Yagyu, and S. Omata, Application of a new tactile sensor to thoracoscopic surgery: Experimen- tal and clinical study, Ann. Thoracic Surg., vol. 60, no. 3, pp. 610614, 1995.

[34] M. Ottensmeyer and J. Salisbury, In vivo data acquisition instrument for solid organ mechanical property measurement, in Proc. Med. Image Comput. Comput.-Assist. Interven., 2001, pp. 975982.

[35] K. Lister, Z. Gao, and J. Desai, Development of in vivo constitutive models for liver: Application to surgical simulation, Ann. Biomed. Eng., vol. 39, pp. 10601073, 2011.

[36] P. Puangmali, H. Liu, L. Seneviratne, P. Dasgupta, and K. Althoefer, Miniature 3-axis distal force sensor for minimally invasive surgical pal- pation, IEEE/ASME Trans. Mechatronics, vol. 17, no. 4, pp. 646656, Aug. 2012.

[37] O. Van der Meijden and M. Schijven, The value of haptic feedback in conventional and robot-assisted minimal invasive surgery and virtual reality training: A current review, Surg. Endosc., vol. 23, pp. 11801190, 2009.

[38] H. Liu, J. Li, X. Song, L. Seneviratne, and K. Althoefer, Rolling indenta- tion probe for tissue abnormality identification during minimally invasive surgery, IEEE Trans. Robot., vol. 27, no. 3, pp. 450460, Jun. 2011.

[39] G. McCreery, A. Trejos, M. Naish, R. Patel, and R. Malthaner, Feasibility of locating tumours in lung via kinaesthetic feedback., Int. J. Med. Robot. Comput. Assist. Surg., vol. 4, no. 1, pp. 5868, 2008.

[40] J. Gwilliam, Z. Pezzementi, E. Jantho, A. Okamura, and S. Hsiao, Human versus robotic tactile sensing: Detecting lumps in soft tissue, in Proc. IEEE Hapt. Symp., 2010, pp. 2128.

[41] M. T. Perri, A. L. Trejos, M. D. Naish, R. V. Patel, and R. A. Malthaner, New tactile sensing system for minimally invasive surgical tumour local- ization, Int. J. Med. Robot. Comput. Assist. Surg., vol. 6, no. 2, pp. 211 220, 2010.

[42] M. Beccani, C. Di Natali, L. Sliker, J. Schoen, M. E. Rentschler, P. Valdastri, Wireless Tissue Palpation for Intraoperative Detection of Lumps in Soft Tissue, IEEE Transactions on Biomedical Engineering, 2014, Vol. 61, N. 2, pp. 353-361

[43] H. Liu, J. Li, X. Song, L. Seneviratne, and K. Althoefer, Rolling indentation probe for tissue abnormality identification during minimally invasive surgery, IEEE Trans. Robot., vol. 27, no. 3, pp. 450460, Jun. 2011

[44] http://en.wikipedia.org/wiki/KelvinVoigt-material

[45] R. S. Dahiya, G. Metta, M. Valle, and G. Sandini, Tactile sensingFrom humans to humanoids, IEEE Trans. Robot., vol. 26, no. 1, pp. 120, 2010.

[46] M. H. Lee and H. R. Nicholls, Tactile sensing for mechatronics: A state of the art survey, Mechatronics, vol. 9, no. 1, pp. 131, 1999.

[47] Pressure Profile Systems, Inc. (2012, Nov.). [Online]. Available: http://www. pressureprofile.com/

[48] Weiss RoboticsTactile sensors. (2012, Nov.). [Online]. Available: http://www. weiss-robotics.de/en/english/technology/tactilesensors.html

[49] A. M. Dollar and R. D. Howe, A robust compliant grasper via shape deposition manufacturing, IEEE/ASME Trans. Mechatron., vol. 11, no. 2, pp. 154161, 2006.

[50] M. Beccani, C. Di Natali, C. E. Benjamin, C. S. Bell, N. E. Hall, P. Valdastri, Wireless Tissue Palpation: head characterization to improve tumor detection in soft tissue, Sensors and Actuators: A Physical, 2015, Vol. 223, pp. 180-190

[51] Tenzer, Y., Jentoft, L.P.,Howe, R.D.The Feel of MEMS Barometers: Inexpensive and Easily Customized Tactile Array Sensors. IEEE Robotics and Automation Magazine, IEEE Vol21 ,Iss: 3

[52] Jentoft, L.P. Tenzer, Y. , Vogt, D., Jia Liu, Wood, R.J., Howe, R.D. Flexible, stretchable tactile arrays from MEMS barometers. Advanced Robotics (ICAR), 2013 16th International Conference.

[53] D. Gray, J. Tien, and C. Chen, High-conductivity elastomeric electronics, Advanced Materials, vol. 16, no. 5, pp. 393397, 2004. [Online]. Available: http://dx.doi.org/10.1002/adma.200306107

[54] D. Brosteaux, F. Axisa, M. Gonzalez, and J. Vanfleteren, Design and fabrication of elastic interconnections for stretchable electronic circuits, Electron Device Letters, IEEE, vol. 28, no. 7, pp. 552 554, july 2007.

[55] D. Gray, J. Tien, and C. Chen, High-conductivity elastomeric electronics, Advanced Materials, vol. 16, no. 5, pp. 393397, 2004. [Online]. Available: http://dx.doi.org/10.1002/adma.200306107

[56] S. Lacour, J. Jones, S. Wagner, T. Li, and Z. Suo, Stretchable interconnects for elastic electronic surfaces, Proceedings of the IEEE, vol. 93, no. 8, pp. 1459 1467, aug. 2005.